Faculdade de Engenharia da Universidade do Porto

Flexible Resistive Switching Devices for Neuromorphic Applications

Catarina Campos up202103359

Dissertação realizada no âmbito do
Mestrado em Engenharia Biomédica

Orientador: Doutora Catarina Dias
Co-orientador: Professor Doutor João Ventura

17/07/2023

Abstract

The von Neumann's digital architecture, in which the memory unit is structurally separated from the processing unit is the process used in conventional digital computers. However, with the rapid evolution of technology, resulting in the increase of the data size to be processed, noteworthy costs in energy and time are suddenly becoming insuperable, constituting the bottleneck of this technology.

New computer paradigms are starting to appear in order to fight these constrains, as is the case of memristors, a novel class of devices showing resistive switching. These follow the process based on the human brain functioning, where the memory itself constitutes the place where data is stored and processed, eliminating the issues that arise with the movement of data between the separated units. Moreover, since these are centered on the transition between two or more states of resistivity, they present an auspicious contender for the capability of mimicking brain functions once this switching behavior resembles synapses. These characteristics make them a great candidate to substitute von Neuman's architecture, as well as a great option to be used in implantable neuro devices. On the other hand, most available implantable devices are rigid and since the human body is mostly composed of soft tissues, this may come as an obstacle to their interface, communication, and adaptability.

The main proposal of this dissertation is the fabrication of resistive switching devices on top of flexible and biocompatible substrates, for neuromorphic applications. Here, resistive switching devices were successfully fabricated using scalable spin-coating and sputtering techniques. The device stacks consisted of an active layer composed of PMMA embedded with TiO_2 or ZnO nanoparticles, deposited onto a flexible and biocompatible PET/ITO substrate. Tungsten electrodes were used as the top electrode, while ITO served as the bottom electrode. The fabricated devices exhibited bipolar resistive switching behavior, with the ability to switch between high-resistance and low-resistance states under low amplitude applied voltage. The resistive switching mechanism was attributed to the valence change mechanism, where a positive polarity voltage led to a transition from low-resistance to high-resistance state (RESET), and a negative polarity voltage caused the transition from high-resistance to low-resistance state (SET). Additionally, the devices demonstrated satisfactory endurance,

retention, and neuromorphic properties. Long-term potentiation and long-term depression were also achieved, which are crucial aspects of the learning process. Future work should focus on validating the devices with neural signals, leveraging their potential for nonvolatile memories and artificial arrays in wearable and implantable applications.

Resumo

A arquitetura digital de von Neumann, na qual a unidade de memória está estruturalmente separada da unidade de processamento, é o processo utilizado nos computadores digitais convencionais. Contudo, com a rápida evolução da tecnologia, há um grande aumento no tamanho dos dados a processar, resultando em notáveis custos de energia e tempo.

Novos paradigmas começam a surgir para combater estes constrangimentos, como é o caso dos *memristors*, uma nova classe de dispositivos que mostram comutação resistiva. Estes seguem o processo baseado no funcionamento do cérebro humano, onde a própria memória constitui o local onde os dados são armazenados e processados, eliminando as questões que surgem com o movimento de dados entre as unidades separadas. Além disso, como estão centrados na transição entre dois ou mais estados de resistividade, apresentam-se uma grande capacidade de imitar as funções cerebrais uma vez que este comportamento de comutação se assemelha a sinapses. Estas características fazem deles um grande candidato para substituir a arquitetura de von Neuman, bem como uma grande opção a ser utilizada em dispositivos neuro implantáveis. Por outro lado, a maioria dos dispositivos implantáveis disponíveis são rígidos e uma vez que o corpo humano é composto principalmente por tecidos macios, isto pode ser um obstáculo à sua interação e adaptabilidade.

A principal proposta desta dissertação é o fabrico de dispositivos de comutação resistiva sobre substratos flexíveis e biocompatíveis, para aplicações neuromórficas como o desenvolvimento de memórias não voláteis e matrizes artificiais. Neste trabalho, os dispositivos foram fabricados com sucesso utilizando técnicas de spin-coating e sputtering. As camadas que os constituem são compostas por PMMA incorporado com nanopartículas de TiO_2 ou ZnO, depositadas num substrato flexível e biocompatível de PET/ITO. Elétrodos de tungsténio foram utilizados como elétrodo superior, enquanto o ITO foi utilizado como elétrodo inferior. Os dispositivos fabricados exibiram um comportamento bipolar de comutação resistiva, com a capacidade de alternar entre estados de alta e baixa resistência sob tensões de baixa amplitude. O mecanismo de comutação resistiva foi atribuído ao mecanismo de mudança de valência, onde uma tensão de polaridade positiva levou à transição do estado de baixa resistência para o estado de alta resistência (RESET), e uma tensão de polaridade negativa causou a transição do estado de alta resistência para o estado de baixa resistência (SET). Além disso, os dispositivos demonstraram uma resistência satisfatória, retenção e propriedades neuromórficas. Apresentaram ainda uma evidente potenciação e depressão, que são aspectos cruciais do processo de aprendizagem e comportamento neuromórfico. Trabalhos futuros

devem-se focar na validação dos dispositivos com sinais neuronais, aproveitando o seu potencial para memórias não voláteis e matrizes artificiais para aplicações de colocação junto ao corpo e implantáveis.

Acknowledgments

First, I would like to express my deepest gratitude to my parents for their unwavering support throughout my entire life. Thank you for allowing me to pursue my degree and my dreams, for always being there for me and for accepting and encouraging me to be true to myself. I am truly grateful for your love, understanding, and eternal patience for dealing with me before my morning coffee. Your guidance and presence have played an instrumental role in shaping the person I am today.

I would like to extend a special thank you to my brother, who has been my constant source of inspiration and a role model in both academic and personal aspects of my life. Your determination, perseverance, and achievements have motivated me to strive for excellence and to believe in myself.

I am immensely grateful to my supervisor Doctor Catarina Dias for her guidance, expertise, and continuous support throughout the course of my dissertation. Her insightful feedback and valuable suggestions have been invaluable in shaping the direction and quality of my work. I would also like to extend my gratitude towards my co-supervisor, Professor João Ventura, for the invaluable help, advice, and guidance extended throughout my dissertation.

I would also like to extend my appreciation to PhD students Henrique and Andreia for their attentive eyes and constant availability to help me navigate through challenges and troubleshoot problems and for all the Python scripts that saved me a lot of time.

Furthermore, I would like to thank IFIMUP for graciously welcoming me, a foreigner from another faculty. The opportunity to join your research group has broadened my horizons in subjects that I had not dealt with before and provided me with a rich learning environment.

To the friends from my heart, who have been with me since kindergarten, and those who reclaimed their place later in my life, you all have become an integral part of my journey, thank you for your unwavering friendship and support, and for always knowing how to deal with my very stressful mind. Your presence, laughter, and encouragement have made the challenges more bearable and the successes more meaningful. I am grateful for the memories we have created together, and I look forward to the continued bond we share.

Yours truly,

Catarina Campos

Página em branco

"Assim como falham as palavras quando querem exprimir qualquer pensamento,
Assim falham os pensamentos quando querem exprimir qualquer realidade.
Mas, como a realidade pensada não é a dita mas a pensada,
Assim a mesma dita realidade existe, não o ser pensada.
Assim tudo o que existe, simplesmente existe."

Alberto Caeiro, 1917

Página em branco

Contents

Página em branco

List of figures

Página em branco

List of Tables

Página em branco

Acronyms, Abbreviations and Symbols

ABsyn	Artificial-to-Biological synaptor
Ag	Silver
Al	Aluminum
Au	Gold
BAsyn	Biological-to-Artificial synaptor
BE	Bottom Electrode
BMI	Brain-Machine Interfaces
C	Capacitor
Cu	Copper
DOD	Drop-on-demand
ECM	Electrochemical Mechanism
EHD	Electrohydrodynamic
EPSPs	Excitatory-postsynaptic potentials
I	Electric current
L	Inductor
ITO	Indium Tin Oxide
M	Memristor
OMD	Organic Memristive Devices
PEO	Polyethylene Oxide
PEN	Polyethylene Naphthalene
PET	Polyethylene Terephthalate
PMMA	Poly(methyl methacrylate)
Pt	Platinum
q	charge
R	Resistor
SEM	Scanning Electron Microscopy
Si	Silicon
SNN	Spiking Neuron
TE	Top Electrode
Ti	Titanium
TiN	Titanium nitride
TiO_2	Titanium Dioxide
V	Voltage
VCM	Valence Change Mechanism

VLSI	Very-large-scale-integration
W	Tungsten
XRD	X-ray diffraction
Zn	Zinc
ZnO	Zinc Oxide
φ	Magnetic Flux

Chapter 1

Introduction

Nowadays conventional digital computers follow the process of Von Neumann's digital architecture, in which the data to be handled must be moved back and forth between the place where it is stored (the memory unit) and where it is processed (the processing unit) [1]. However, due to the structural separation of the processing and memory units, as well as the increase in size of the data to be processed, this process incurs noteworthy costs in energy, time, and potential, constituting the bottleneck of this architecture. The increasing disparity between the speed of the mentioned units is also to be taken note of and is typically referred to as the Memory Hall.

These constrains are reaching a point in which it stops the evolution of computing systems and so alternatives started being implemented, like the use of a couple of thousand processors in parallel or custom-designed application-specific processors. However, although easing the problems at hand, these do not seem to overcome them [2].

An alternative that seems promising is the one based on the human brain structure, where the memory itself constitutes the place where data is stored and processed, eliminating the issues that arise with the movement of data between the separated units, commonly known as In-Memory Computing.

As is known, the brain is the most complex organ of the human body and the one we know less about. It commands every single aspect of our lives, what we learn, think, feel and do, in an intricate way. The key to this very complex system is the way neurons communicate with each other, through synaptic connections, leading to large connectivity between them and thus presenting a highly parallel processing power [3], forming neural networks.

Therefore, the brain presents a different computing paradigm, but much more powerful configuration than modern computers, with better memory retention and learning capabilities, while presenting lower power consumption [4]. Thus, research in developing devices to mimic brain functions is extremely important to progress in the big data world.

Given the complexity and importance of the human brain, any neurological disorder disrupts life in various implacable ways. With the current life expectancy growing each year, new disorders and conditions are starting to appear and grow, as is the case of neurological ones. To help mitigate and treat these problems, some implantable devices have been discovered and implemented to treat neurological disorders and damages, like for Parkinson's

Disease with deep brain stimulation and robotic prostheses with neural interfaces. However, despite the continuous development of the topic, there are intrinsic differences between biological tissues and electronic devices. Tissues and organs from our body are mostly soft and of very high-water content, oppositely, most available implantable electronic devices are rigid. These differences impose various difficulties when it comes to interfaces between biology and electronics [5].

A novel class of devices has been proven to be able to respond to this quest for a new computing paradigm, able to perform real-time adaptative computing and thus help fill the gap in implantable devices. Resistive switching devices, based on the transition between two or more states of resistivity, present an auspicious contender for the capability of mimicking brain functions since this switching behavior resembles synapses [6]. Furthermore, these devices present a high read/write speed, excellent endurance, fast switching speed, low programming voltage, and high storage density capability compared to regular digital memories [7], making them a great candidate to substitute Von Neuman's Architecture, as well as a great option to be used in implantable devices.

To accommodate brain physiology these devices may be produced using flexible substrates, to allow their correct placement and stability. Moreover, to prevent rejection of the implants, they must be created using biomaterials, to allow their biocompatibility. Furthermore, biomaterials have been proven to present some mechanical properties that make them ideal for implantable devices, such as surface elastic response, adhesion, and elasticity, and electrical properties like moderate to high mobility of charge carriers, thermal stability across a varying temperature range, and high bandgap between the energy levels which make them ideal for the fabrication of flexible electronic devices [8].

Hence, the need for biocompatible and implantable devices, preferably soft and humid, capable of emulating synaptic networks, is the main motivation for this dissertation, through the production of resistive switching devices on top of flexible substrates.

1.1 - Objective

This dissertation's main objective is to fabricate flexible resistive switching devices on top of flexible and biocompatible substrates, for neuromorphic applications such as the use of nonvolatile memories and artificial neuromorphic arrays for wearable and implantable applications.

The experimental part of this dissertation will be divided into two main steps, the fabrication of the devices and their characterization. The fabrication step is mainly divided into two, the deposition of the material, in which methods like spin-coating and drop casting will be used, and the definition of nano structures, with the use of sputtering.

Different types of material will be tested in order to get to the ideal device. When it comes to the active switching layers, polymers and metal oxides will be tested. Silver, tungsten, aluminum and indium tin Oxide (ITO) will be used as electrodes. Regarding the substrates, some tests might be performed in rigid substrates before entering the flexible ones, where PET will be tested.

1.2 - Structure of the dissertation

The dissertation in progress will be composed of the following topics by the order presented. In Chapter 1, the introduction to the dissertation will be presented, followed by the state-of-the-art in Chapter 2. In Chapter 3, the process from which the devices will be fabricated will be thoroughly depicted. The results obtained will be discussed and presented in Chapter 4, followed by the conclusion of the dissertation in Chapter 5.

Página em branco

Chapter 2

State-of-the-art

2.1 – Resistive Switching Behavior - Memristors

Nowadays, computing systems are built under Von Neumann's architecture, with a structural separation of the processing and memory units, which has been known to be the cause of some issues that started to appear with the rapid computer science evolution.

An alternative architecture is the one based on the human brain structure, known as In-Memory Computing, in which the place where the data is stored is also where it is processed.

One emerging option in this kind of computing is resistive random access memory (RRAM), also known as memristor based memory devices [9]. In these, information is stored through differences in atomic arrangements or in the different orientations of the ferromagnetic metal layers. Their capacity to switch between high and low resistive states, allows a non-volatile storage capability with a range of conductance states [2]. This kind of computing uses an electronic component, the memristor, that will be presented in the following sections.

Chua, in 1971, presented the memristor or memory resistor (M) as the 4th fundamental circuit element, besides the resistor (R), capacitor (C), and inductor (L).

He discovered that six different mathematical equations related the four fundamental circuit variables (electric current - i, voltage - v, charge – q, and magnetic flux - φ). Five of them were already portrayed and known, three that defined the fundamental elements (R, C and L) and the other two that defined the Faraday's law of induction (q as the time integral of the current and φ as the time integral of voltage). However, the mathematical relation between q and φ existed, but there was something missing to prove it. Thus, he stated that there should be a 4th element that provided this relation, which he determined to be the Memristor, with Memristance M [10]. The four fundamental circuit elements: resistor, capacitor, inductor and memristor, together with the six equations that portray its relations are represented in Figure 1.

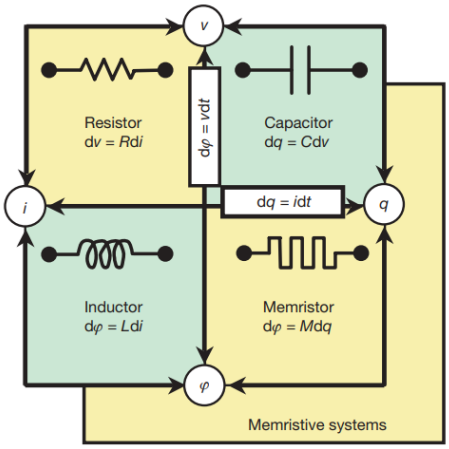

Figure 1 - Representation of the four fundamental circuit elements; resistor, capacitor, inductor and memristor and its relations. Retrieved from [11]**.**

2.1.1 Behavior

The memristor can be characterized as a resistor with memory, in which its value of resistance is determined by the charge flowing through it [12]. It is a passive element with two terminals presenting exceptional nonlinear features, which the other three basic circuit elements and their combinations cannot duplicate.

The four elements' behavior in the I-V domain is represented in Figure 2. Like it is commonly known, the resistor presents a linear relationship between voltage and current, whilst the capacitor and inducer are represented through a circular shape with 90º phase difference. Looking at the memristor representation, a very characteristic curve can be observed, a pinched hysteresis loop, with crossing in the referential zero. The current hysteresis response to a periodic voltage is the fingerprint of memristor devices, reflecting the effect of short-term memory it presents [13].

The resistance of a memristor can be programmed to be in low or high state, by applying SET and RESET pulses. This way, the resistance increases or decreases depending on the polarity of the current or the applied voltage. The removal of the source of excitation does not make a change in the resistance, property that allows the memristor to act as a memory.

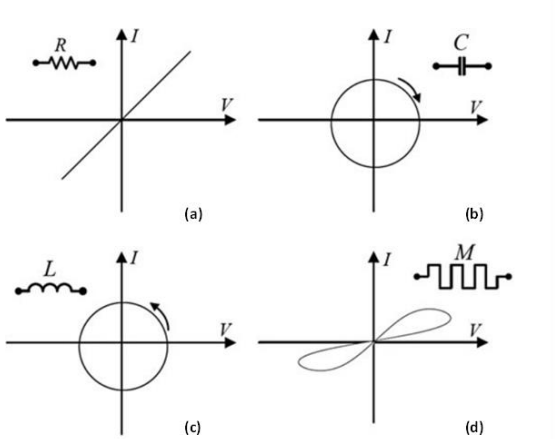

Figure 2 - Representation of the characteristic curve of the four circuit elements in the I-V domain: (a) Resistor; (b) Capacitor;(c) Inducer; (d) Memristor. Adapted from [13]**.**

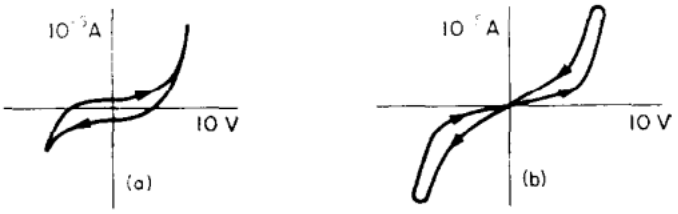

Figure 3 - Hysteretic curves observed in the behavior of a titanium dioxide film. Adapted from [14]**.**

2.1.2 History

Although the first device called memristor, was only produced by Strukov et al. in 2008, using a titanium dioxide (TiO_2) thin film [11], the memristor behavior was previously observed in 1968 by Argal [14], when the current-voltage behavior of a titanium dioxide film was observed through a series of hysteretic curves, as can be observed in Figure 3.

Then, in 1971, Chua was the first to present the ideal model of memristor, and the first to give it its name. He proved that when the electrical flux was increased over a threshold, the device switched from one resistance to the other, and reverted to the original state when the flux decreased over the same threshold, producing the hysteretic curve. Although he was not able to produce an actual device, he proved in the circuit-theoretic that it was possible to produce a memristor with no internal power supply [10].

Finally, in 2008, Strukov et al [15] produced the first physical model for a memristor. It consisted of thin semiconductor film of TiO_2 in between two metal contacts, as can be observed in Figure 4.

This film had one region with a high concentration of dopants with low resistance and a region with almost zero dopant concentration and higher resistance. By applying an external source of energy, the dopants drift, moving the boundary between the two regions and thus causing changes in the resistance. They were able to produce the first memristor with an hysteretic behavior in the I-V domain, although this behavior in the TiO_2 film had already been proved by Argal [14].

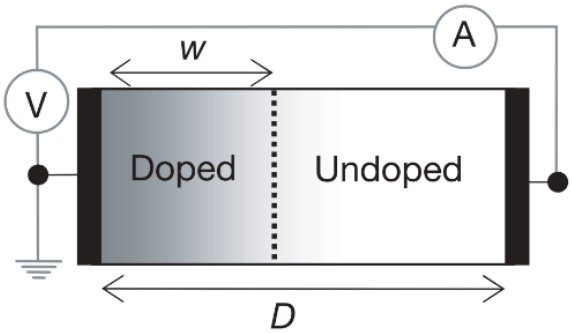

Figure 4 - Schematic representation of the first memristor proposed by Strukov et al. Retrieved from [15]**.**

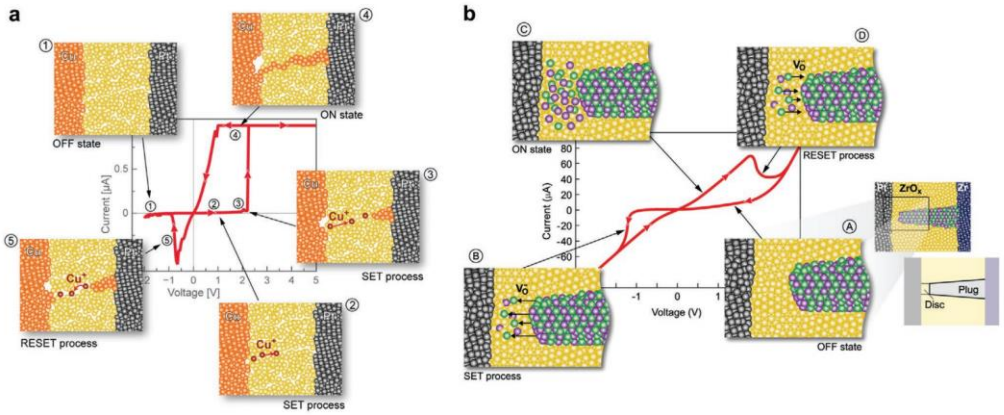

Figure 5 - Mechanism of ECM (a) and VCM (b) RS mechanisms. The I-V curves characteristic from each mechanism is also represented. Adapted from [16]**.**

2.1.3 Classification of Memristors – Switching Mechanisms

Memristors can be based on three different switching mechanisms, ionic switching, ferroelectric and phase change.

2.1.3.1 Ionic switching

This type of switching mechanism is the most prevalent when it comes to memristors. Its main characteristic is centered on the movement of ions between the two electrodes and can range from oxygen vacancies to active metal cations and anions. This mechanism is mainly divided into two, the Electrochemical Mechanism (ECM) and Valence Change Mechanism (VCM).

(A) Electrochemical Mechanism – ECM

This mechanism is based on a common electrochemical oxidation-reduction process. It relies on the formation and rupture of metallic films that are in short-circuit (SET process, leaving them in LRS (ON)) or disconnected (RESET, leaving them in HRS (OFF)). These devices are usually composed of an electrochemically active electrode (Ag for example), a switching film (usually with an oxide, chalcogenide or single-element material, like Si) and an inert electrode (like ITO or Pt).

In Figure 5 (a), 1 to 5, is depicted the process of the ECM mechanism. When an external voltage is applied to the active electrode (Cu in this case), the metal atoms oxidize and transform into the corresponding ions (Cu^+), causing them to diffuse through the active layer (2). When in this layer, they are reduced to their atom form (Cu), combine with each other (3), and form a conductive filament up until the inert electrode (PT in this case) (4). This sends the memristor to a low resistance state. In order to get it into a high resistive state, the filament between the electrodes must be ruptured, by applying a reverse bias, making the atoms transform into their oxidized form (5). The typical I-V curve characteristic from this mechanism is also represented, where the direction of the arrows must be taken into account [16].

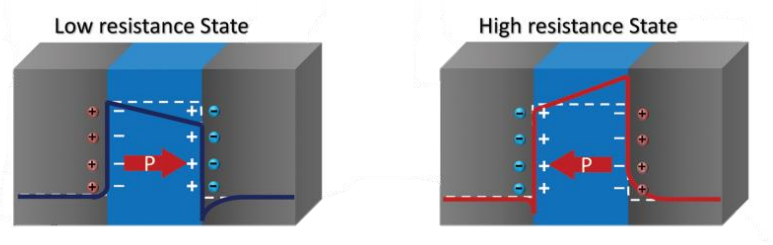

Figure 6 - Schematic representation of the principles behind memristors based on the Ferroelectric Mechanism. Adapted from [17]**.**

(B) Valence Change Mechanism - VCM

This mechanism is based on the rearrangement of vacancies in the active layer, that determines the state of the device. These are usually formed by an ohmic electrode (Ti, Ta, ITO), a switching film (preferably an oxide) and an inert electrode presenting a higher-work function than the active layer.

In Figure 5 (b), A to D it is represented the VCM typical mechanism. Contrary to the ECM mechanism, the states are not defined by the complete dissolution of the filaments as they remain largely intact (plug), but because of a barrier (disc) between the inert electrode and the tip of the filament. By applying a positive bias, there is an exchange of oxygen (ions/atoms) between the active electrode and the active layer, and the elements that are in the disc join the plug, in direction to the inert electrode (C). This triggers redox reactions in the disc (D), switching the device to a HRS (A). When applying the reverse voltage, the elements in the disc that joined the partial filament, return to their original site, leaving the memristor in a Low Resistance State (B) [16].

By looking at the I-V curve characteristic of this mechanism and comparing it to the ECM one, it can be seen that the direction of the arrows are the exact opposite. In the VCM mechanism, a positive bias leaves the devices in a HRS, a RESET process, whereas in the ECM one, the devices is put in a LRS with a positive bias, a SET process.

2.1.3.2 Ferroelectric

Ferroelectric tunnel junctions are a kind of device that uses this mechanism. It is constituted by a ferroelectric insulator material, separating two metal electrodes. Some processes can occur with these, as quantum electron tunneling is the dominating one. The movement of electrons through a potential barrier in the insulator material is the central point of this mechanism. Depending on the alignment of polarization in the material, the stream of electrons is changed, resulting in the production of tunnel electro-resistance effect. When a bias is applied across the two electrodes, the potential at the insulator decreases or increases depending on the direction of the polarization, resulting in significant resistance changes [18], which can be observed in Figure 6.

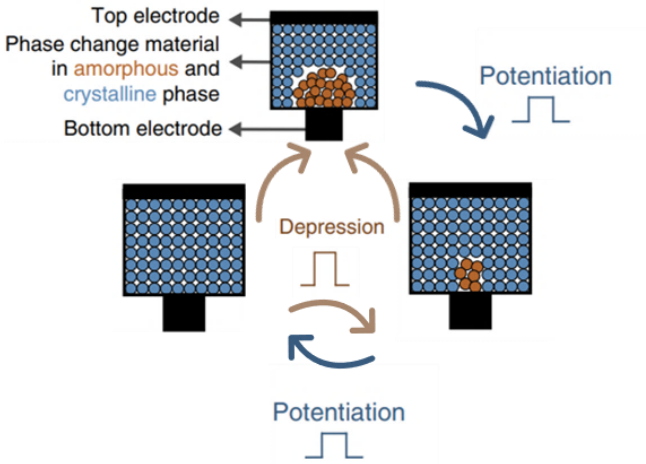

Figure 7 - Schematic representation of the principles behind memristors based on the Phase Change Mechanism. Adapted from [19].

2.1.3.3 Phase Change

In this kind of mechanism, a change in the phase of the material is what makes its resistance state change. When a voltage is applied between the top and bottom electrode and a depression pulse is sent, a heating process is promoted, gradually heating the phase change material, changing it from a crystalline to an amorphous phase, resulting in a change in the resistance of the memristor. This way, the amorphous phase is usually associated with a high resistance state, whereas the crystalline phase is related to a low resistance state once conductivity rises due to the charge carriers' localization in the crystalline state. To return the memristor to a crystalline (low) state, a potentiation adjusted pulse must be applied, crystallizing once again the phase change material layer [18][19]. A schematic representation of this mechanism is presented in Figure 7.

2.1.4 Neuromorphic properties of memristors - Mimicking brain behavior

The most important brain cells are neurons. Neurons communicate with each other through synapses, and this is what allows us to think, keep memories and overall command our body. Synapses can process, store and transmit information simultaneously, providing the substrate for synaptic computing and learning.

Figure 8 shows the schematic representation of a synapse. Synapses usually start with action potentials, that trigger the opening of voltage-gated calcium channels. The activation in these channels makes the presynaptic neuron release neurotransmitters. These blind the receptors on the postsynaptic neuron, causing changes in the current/potential [20].

Synapses and memristors end up presenting with similar sandwich structures and operating mechanisms. The pre- and postsynaptic neurons can be comparable to the top and bottom electrode of the memristor and the dopants in the semiconductor film are comparable to the neurotransmitters. Based on these assumptions, can be said that the memristor has a neuromorphic behavior, once it resembles brain functions and, thus, should be capable of being used in artificial synapses to construct artificial neural networks [12].

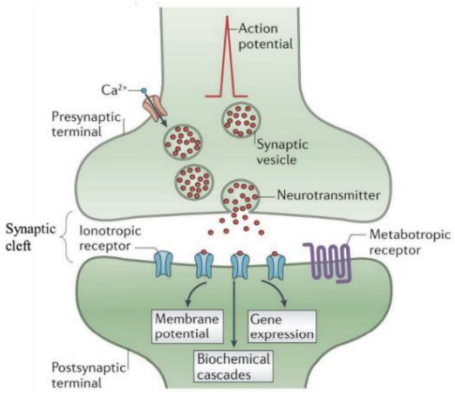

Figure 8 - Synapse's schematic representation. Retrieved from [20]**.**

2.1.5 Applications of Memristors

After the first step taken by Strukov et al [15], various approaches in the different uses of the memristor started to appear, such as their use in nonvolatile memory arrays, analog and digital modulation and neuromorphic computing circuits.

A. Memristor as an Interface between biological and artificial neurons

Memristors have also been found to act as an interface between biological and artificial neurons. In 2020 Serb et al, reported to be able to demonstrate linking between silicon spiking neurons (artificial) and brain neurons in both directions, using two memristive connections, that emulate synaptic function [21]. The artificial-to-biological synaptor (ABsyn), is composed of a TiOx commercial memristor coupled to a metal-thin film TiO_2 microelectrod that provides the connection between a very-large-scale-integration (VLSI) spiking neuron (SNN) and a biological neuron from a rat, in culture. This link, is able to emulate a brain synapse both when it comes to transmission and plasticity. The artificial neuron starts by sending a pre-synaptic depolarization to the memristor (MR1). The resistive states from the memristor are translated into adjustable voltage stimuli, through CME, one of the elements of the multielectrode array, CMEA, producing postsynaptic depolarizations in the biological neuron, resembling native excitatory-postsynaptic potentials (EPSPs). The biological-to-artificial synaptor (BAsyn) functioning ends up being similar to the previously mentioned one. The signals sent by the biological neuron are recorded in the CMEA and sent to the memristor MR2, which sends it to the artificial neuron [21].

B. Memristor as an Interface between two live biological neurons

In 2018 Juzekaeva et al, were able to couple two live neurons from brain slices through the use of organic memristive devices (OMD). In this experiment, a nonconnected pair of neurons from rat brain slices were connected through an OMD paired with an electronic circuit, which functioned as a synapse. The structure of the OMD comprised a conducting polymer (polyaniline) and a solid electrolyte—lithium salt doped polyethylene oxide (PEO). The memristance features were achieved through the conductivity difference in the oxidized and reduced polyaniline forms [22].

C. Memristor used as storing and processing units in neuronal applications

Besides being able to connect neurons and emulate synapses, memristors can also be used to store and compute fast blasts of events, as is the case of spikes produced by neurons. Gupta et al in 2016 were able to produce an array comprising a memristive device capable of storing information coming from transduced neuron spikes recorded through a multielectrode array, when it comes to amplitude and frequency. This proved the potential of memristors to be used as a low scale, energy-efficient processors for brain-chip interfaces [23]. The external frontend is where the neuronal signals are acquired and amplified. The waveform resultant from the signal sent to the software is sent to the memristor and the reading circuit periodically measures its resistive state. When changes occur, these are sent once again to the software and extracted as spikes [23].

Following this application, Liu et al proposed in 2020 the use of memristors not only in the reception and storage of neural signals but also in their analysis for next-generation brain-machine interfaces (BMI). They proposed a future BMI incorporating a memristor-based system capable of storing and analyzing neural signals. First, neural probes acquire activities produced by neurons and send it to the memristor array, where they are stored, analyzed and sent to the brain again as commands for human or computer effectors [24].

Published last year (2022), Dias et al proved for the first time the use of a memristive system to acquire different patterns of neural signs and act depending on them, working as an artificial synapse. This project presents an envisioned system composed of a memristor linked to a source and a target. In the beginning the memristor is in the high resistive state (OFF), resembling a low synaptic connection. When the source electrode receives signs of activity in a designed pattern, the target population is electrically stimulated, inducing them to fire to the source population. When the spiking rate lowers to baseline activity, the connection is dissolved [25].

2.1.6 Types of materials used for memristors

Memristors main components are the active components, in the dielectric layer (Active Insulating Layer), which are sandwiched between two electrodes, on top of a substrate.

A. Active components

The main active components of memristors can be composed of inorganic, organic, and inorganic-organic materials [12]. The organic components include biomaterials from natural sources, like lignin [26], egg albumen [27], and potato starch with chitosan [28], and polymer materials such as glucose [29] and polydopamine [30]. The inorganic materials, which are the most commonly studied, comprise transition metal oxides, including TiO_2 [31], $SrTiO_3$ [32][33], NiO [34], CuO [35], ZnO [36], MnOx [37], Ta_2O_5 [38], Ti_2O_5−x/TiOy [39], and chalcogenides [40]. Some inorganic-organic materials have also been used to produce memristors, like some perovskites [41], [42].

B. Electrodes

The selection of the right electrodes to be used is also fundamental to the memristors' functioning. Depending on the type of switching mechanism (mentioned in Section 2.1.3.1), the proper active electrode is crucial to the performance of the memristors. Thus, it should be chosen depending on the materials used in the active layer. Nevertheless, for all mechanisms it is crucial that one of the electrodes is electrochemically active. This way, most used materials for their production include metals such as Ag, Cu, Ti, Zn, Al and their alloys, once they can promote oxidation of metal ions, vital to change the memristor's resistance [43]. However, some electrochemically nonreactive materials have also been reported to be used such as Au and Pt [43], as well as graphene, which presented excellent physical and chemical properties, such as superior electrical conductivity and good tensile strength [44].

C. Substrates

The substrate on top of which is fabricated any electronic component is a very important part to be taken into consideration. It is responsible for factors such as cost-effectiveness, mechanical and chemical characteristics or even production feasibility [45].

The most common substrates used are rigid such as Si, for its lower price and proper mechanical and electronic properties.

However, especially when talking about implantable devices, rigid substrates are not the best option, since they are not conformable with biological systems. Therefore, these should be produced on top of flexible substrates. Once demonstrated they could be an asset for some applications, memristors produced in flexible substrates have been an area of extensive research in the past few years.

When talking about flexible substrates they must present some important characteristics apart from scalability, weight and cost such as:

(i) Mechanical: sturdy mechanical flexibility and dimensional stability, especially when it comes to plasticity and its ability to return to the original shape.

(ii) Electrical Conductivity: since one of the memristor's electrode is deposited right on top of the substrate, it must not interfere with the ability of the devices to switch resistance states.

(iii) Chemical Stability: depending on the type of fabrication process the memristor undergoes, it might include the exposure to strong chemical gases and solvents, so the substrate must be inert to them.

(iv) Barrier: some type of memristors might be susceptible to degradation when in contact with oxygen and moisture, so in order for the substrate to serve as a barrier it must prevent penetration from external substances

(v) Thermal and Thermomechanical: in addition to chemical changes, in the fabrication process of memristors, they undergo through thermal changes, so when picking a substrate, one must take into account the thermal expansion and transition temperature of the material.

(vi) Surface Uniformity: to prevent electrical short-circuiting in the memristor fabrication, uniformity of the surface of the substrate is of extreme importance in order to provide uniform coating of different layers [45].

As for the Flexible substrates, they can be divided into three main groups:

(i) Plastics and polymers

Typically, in the fabrication of electronic devices, most flexible substrates used are based on polymers, such as polyethylene terephthalate (PET) and polyethylene naphthalene (PEN). However these do not seem to perform well in higher temperatures, which constitutes a disadvantage for implantable devices, since most physiological processes can reach elevated temperatures [45].

(ii) Metal Films

As alternatives to plastic substrates, that are more compatible with higher temperatures are metals likes titanium [46] and stainless steel [47], also presenting interesting mechanical, electrical and chemical resistance properties.

(iii) Other substrates

Another material that has been shown some applications as a flexible substrate is ultrathin glass, which also withstands higher temperatures and has great mechanical stability, as well has allowing moisture penetration [48]. Paper and cellulose bases substrates, have also been reported as options for flexible substrates in a range of electronic applications, presenting with very low cost and weight and also environmentally friendly properties [49]–[52]. Another novelty candidate for a flexible substrate is mica, which presented promising results in terms of flexibility and thermostability [53].

In Table 1 it is presented the comparison between the main flexible substrates mentioned. As can be seen, they all present great qualities when used as flexible substrates, but all of them have a certain category with worse performance.

Table 1 - Comparison between the use of different materials as substrates. Adapted from [45].

Properties	Plastics/ Polymers	Metal Foils	Ultrathin Glasses	Paper [51]	Mica [53]
Scalability	Good	Good	Poor	Good	Very good
Weight	Light	Heavy	Moderate	Variable (depends on the filler used)	Moderate
Thickness	Thin	Thin	Variable	Thin	Thin
Cost	Low	High	High	Very Low	Low
Flexibility	Good	Good	Poor	Good	Good
Barrier Property	Poor	Good	Good	Poor	Good
Thermal Durability	Low	Good	Good	Good	Very good
Surface Uniformity	Smooth	Very Rough	Moderate Roughness	Uniform, but porous	Large Flat Regions

2.1.7 Fabrication Techniques

With their sandwiched configuration, memristors are mostly produced in an array shape of M × N size, with each memristor cell placed in columns and rows, as can be observed in Figure 9. Usually, the bottom electrodes are deposited first on the substrate with an adequate fabrication technique. Then the active layer and the top electrode follows. This fabrication allows the production of more than one memristor in a single attempt. Also, since the spacing between each device seems to be enough, the crosstalk or charge leakage is negligible between and within the layers.

In terms of sizing, the electrodes are in the range of nm to μm width, and the active layer in the nm scale [43].

In the memristor industry, fabrication techniques are usually divided into two main groups, Contact and Non-contact technologies.

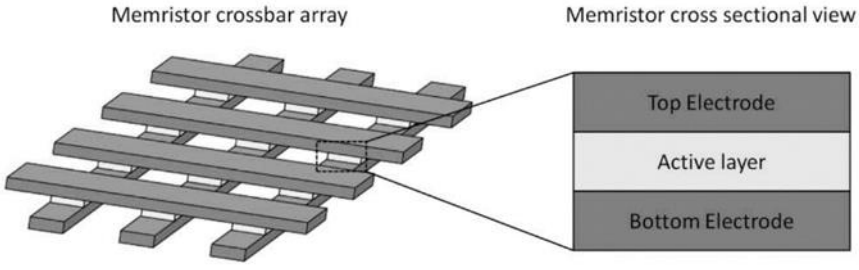

Figure 9 - Typical architecture of memristors produced in a crossbar configuration. Retrieved from [43].

A. Non-contact fabrication

(i) Inkjet printing

This technique consists of a computer-controlled mechanism that commands a printer to deposit inkjet material on the target substrate.

There are two kinds of inkjet printers, piezoelectric and thermal. In the first one, the vibration of a piezo crystal inside the extruding nozzle generates the droplet that is deposited, whereas in the thermal method, the material is heated through applied voltage allowing the extruding to happen in the nozzle [43].

(ii) Aerosol Jet printing

This technique is based on the extruding of the printing material through the pressure of sheath gases.

There are also two ways in which the material can be extruded, pneumatic and ultrasonic. In the pneumatic, the aerosol jet is obtained when a supplied gas is applied to the ink chamber through a tube. This makes the ink rise and be ejected with applied pressure in the shape of micro droplets. In the aerosol ultrasonic jet, the resolution is increased once it allows more manipulation, once the droplets are generated by pressure waves generated by an ultrasonic actuator. Then the gas is applied to the chamber, making the droplets already generated come out through the nozzle [43].

(iii) Electrohydrodynamic technique (EHD)

This technique is based on ink that is ionized through an electrical field and produces a canonical jet. This process is highly controlled through a high-speed camera, and a computer-controlled platen, where the substrate is placed.

EHD can be continuous or drop-on-demand (DOD). The continuous process, continuously deposits the extruding material whilst the drop-on-demand ejects the ink in a controlled motion, monitored through a pulsating voltage. Both have advantages depending on the results wanting to be achieved, once in the continuous, there will be fewer blank spots but more material might be wasted, and in the DOD, in some applications the blank spots might not be that important for the outcome and less material will be wasted [43].

B. Contact fabrication

(i) Screen Printing

This is a very simple and old technique that has been used for a while when it comes to the fabrication of printed electronic devices.

In this technique a screen with a stencil is placed on top of the substrate. Then the printed material is poured on top and squidged to spread to the entire surface. The ink transfers to the substrate according to the pattern on the screen [43].

(ii) Flexography

This technique is based on a cylinder with raised patterns (developed by photolithography) that is attached to a plate. The cylinder picks the ink and transfers it to the substrate on top of the printing plate, in combination with an impression cylinder that pushes the plate towards the top cylinder to help with the pattern transfer [43].

(iii) Spin Coating

This mechanism consists of a motor spinner, a computer controlling unit, to allow the adaptation of the number of revolutions and a vacuum generator to keep the substrate in place during the process.

With the help of a pipette, the material in liquid form is poured on top of the substrate. Secured in place by the vacuum, the substrate is spined and the material spreads over the surface due to centrifugal force. The thickness wanting to be achieved can be easily controlled by the spinning time and speed [43].

Comparing the different techniques mentioned (Table 2), the one with a better range of resolution is screen printing, also presenting with the lowest printing thickness. However, this technology may lead to high roughness of film, requires a high initial setup cost and leads to some material waste, especially when talking about continuous EHD. When analyzing the electrode and active layer fabrication, most of them can do both, except for Spin Coating for electrodes and Screen printing for the active layer, once they are not suitable for these applications.

Table 2 - Comparison between the different Memristor Fabrication Techniques. Adapted from [43], [45]**.**

	Non-Contact Fabrication			**Contact Fabrication**		
	Inkjet	**Aerosol Jet**	**EHD**	**Screen printing**	**Flexography**	**Spin Coating**
Resolution (μm)	15-100	10-100	10-500	30-100	30-80	NA
Thickness (μm)	0.01-0.5	10-15	0.001-0.10	3-30	0.17-8	0.01-10
Speed (m/min)	0.02-5	0.6-1.2	0.1-3	0.6-100	5-180	NA
Material waste	No	No	Yes	Yes	Yes	Yes
Mask Requirement	No	No	No	Yes	No	Yes
Printing Area	Large	Large	Large	Medium	Large	Medium
Electrode Fabrication	Yes	Yes	Yes	Yes	Yes	No
Active Layer Fabrication	Yes	Yes	Yes	No	Yes	Yes

2.2 – Proposed resistive switching structure

The successful fabrication of memristors relies on careful selection and integration of various materials and components to achieve optimal performance. Here is presented the optimal design of the device after thorough testing and refinement, as shown in Figure 10.

The design incorporates a flexible substrate made of Polyethylene terephthalate (PET), enabling the resulting devices to be flexible and conformable to different surfaces and shapes. This flexibility opens possibilities for their integration into wearable electronics and other applications where mechanical flexibility is a crucial requirement.

The choice of Indium Tin Oxide (ITO) as the bottom electrode in the memristor structure offers several advantages. ITO is a transparent and conductive material that provides robust and reliable electrical contact with the substrate with excellent electrical properties.

The active layer of the memristor is composed of Poly(methyl methacrylate) (PMMA) doped with nanoparticles of Titanium Dioxide (TiO_2) and Zinc Oxide (ZnO). These nanoparticles, known for their unique electrical properties, enhance the functionality of the active layer by modifying the charge transport mechanisms within the device. The incorporation of TiO_2 and ZnO nanoparticles in the PMMA matrix enables improved resistive switching behavior and enhances the device's overall performance.

Completing the memristor structure, a circular Tungsten (W) thin film electrode or a W probe are used as the top electrode. Tungsten, known for its exceptional electrical and thermal properties, ensures efficient charge injection and retrieval within the device. The circular W electrode provides a well-defined contact area and enables precise control over the resistive switching behavior of the memristor.

2.2.1 Resistive Switching (RS) in PMMA with nanoparticles

In recent times, hybrid composites combining inorganic and organic components (polymers), specifically those incorporating inorganic nanoparticles (metals, oxides), have shown great promise as viable options for future nonvolatile memory devices [54]. These present a range of advantages such as cost-effectiveness, facile solution-based processing methods such as screen-printing or spin-coating, and the ability to tailor the mechanical, electronic, and optical properties through chemical synthesis. Moreover, by changing the concentration of the nanoparticles in the polymer, makes it possible to finetune the switching properties of the devices [55].

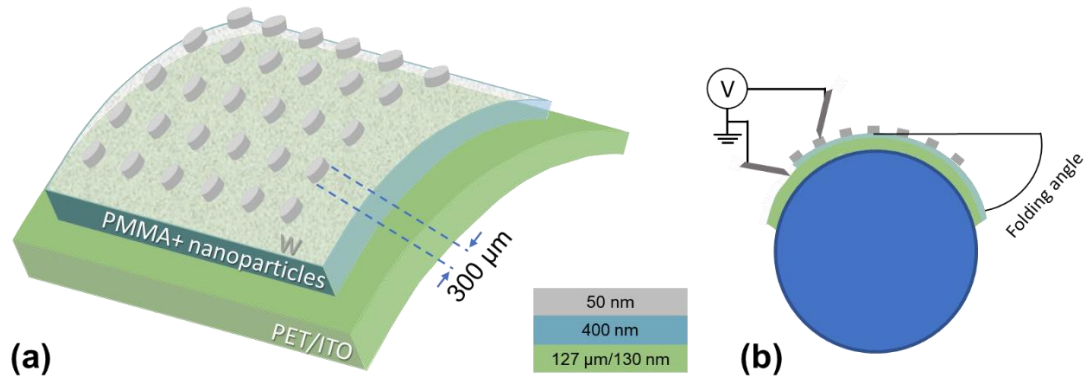

Figure 10 – (a) Schematics of the memristor stack. (b) Schematic representation of the folding measurements. Adapted from [52]**.**

Among the various organic materials investigated for RS, polymethyl methacrylate (PMMA) has emerged as a promising candidate due to its desirable electrical and physical properties, such as high dielectric strength, low cost, and insulator properties [56]. As for the inorganic nanoparticles embedded in the polymer layer, some of those that have been showing evidence of RS are ZnO [57] [58] [59] and TiO_2 [55] [60] [61], with ultra-fast switching speeds (less than 25 ns), substantial OFF/ON resistance ratios (up to 10^5 orders of magnitude), excellent endurance (over 10^5 cycles) paired with prolonged data storage retention (over 10^6 s) .

Given these considerations, stacks of ITO, PMMA with nanoparticles (ZnO or TiO_2), were studied during this work, with refinements on the thickness of the layers and concentration of the particles.

(A) RS in ZnO and TiO_2

RS in RRAM devices with ZnO are based on the valence change mechanism (VCM), which is responsible for the creation and removal of conductive filaments within the device, facilitated by the nano ions transportation of oxygen vacancies and interstitial oxygen ions at the nanoscale in the ZnO layer [62]. Similarly, when in the presence of TiO_2, resistive switching also seems to be based on the VCM effect. VCM occurs due to the migration of oxygen vacancies, from the ohmic electrode to and within the ZnO or TiO_2 film [63].

As mentioned in chapter 2.1.3.1, this is most likely the mechanism happening because the ITO electrode serves as the ohmic electrode, once it has a high oxygen affinity for attracting oxygen ions due to its abundant oxygen vacancies [64]. The active layer contains oxides (which both ZnO and TiO_2 are), and W works as the inert electrode and presents a higher-work function than both ZnO and TiO_2. Most likely, ECM is not happening because neither ITO nor W are particularly electrochemically active.

2.2.2 Biocompatibility of the device

In recent years, there has been an increasing demand for the development of implantable and wearable devices that seamlessly integrate with the human body. The successful implementation of such devices relies not only on their functionality and performance but also on their compatibility with the biological system they interact with. Therefore the biocompatibility of the materials is discussed here, with the ultimate goal of enabling their safe and efficient use in implantable and wearable devices. Understanding the biocompatibility of these devices is a crucial step toward the advancement of implantable and wearable technologies.

PMMA is a widely recognized biocompatible polymer that exhibits excellent chemical stability and low toxicity. It has been proved to be compatibility with living tissues both internal and external [65]. The Polyethylene terephthalate coated with Indium Tin Oxide (PET/ITO) combines the desirable properties of PET, such as flexibility and durability, with the conductive and transparent characteristics of ITO. It has been proved that ITO has great capacities in preventing protein adsorption which demonstrates its biocompatibility [66]. PET is one of the most used polymers in the health sector due to its good biocompatibility [67].

Additionally, we have incorporated Zinc Oxide (ZnO) and Titanium Dioxide (TiO_2) nanoparticles in the active layer. These nanoparticles offer unique electrical properties and have been extensively studied for their biocompatibility in various medical applications [68] [69]. Furthermore, Tungsten (W), is also known for its exceptional stability and biocompatibility [70].

By choosing these biocompatible materials, the aim is to develop memristors that can function reliably within the human body without triggering adverse reactions or compromising the overall health of the individual. However, although all the materials show biocompatibility, they could further be encapsulated in an additional biocompatible material to preserve their characteristics.

Chapter 3

Experimental Methods

3.1 – Solutions Preparation

The flexible switching layer was based on nanoparticles dispersed on a polymeric layer. First the polymer was prepared using 1 g of polymethylmethacrylate (PMMA) powder (average Mw ~ 350000) [71] that was dissolved in 25 mL of toluene in a water bath at 40ºC. Then the nanoparticles, ZnO (<100 nm) [72] and TiO_2 (30 nm Rutile and <100 nm Anatase+Rutile) [73] [74] nanopowders were dissolved on chloroform. Depending on the desired concentration (11%, 20% or 60%), the powders were dissolved in 336 µL, 672 µL and 4032 µL of chloroform. These nanoparticle solutions were then added to 10 mL of the solution of PMMA with toluene. All the solutions underwent a magnetic stirring process until fully dissolved.

All the particles used were purchased from Sigma-Aldrich Co, except for the TiO_2 (30 nm) nanopowder, that came from US Research Nanomaterials.

3.2 – Stack Deposition

The synthetized solutions were both deposited using Spin-Coating and Drop-Casting to define the active layer on top of PET/ITO flexible and transparent substrates, with 60 Ω/sq of surface resistivity and 5 mil (≈127 µm) thickness from Sigma-Aldrich Co [75]. As top electrodes both 5 µm diameter tungsten microtips were used, as well as 50 nm thick and 300 µm in diameter circular tungsten electrodes defined by Sputtering.

3.2.1 Spin-Coating

Spin-Coating (mentioned in Section 0) was used to deposit the active layer on top of the bottom electrode. This method was chosen as it is relatively simple and cost-effective compared to the other options in the same thickness range, like inkjet or flexography. Moreover, this is one of the most commonly used methods for forming high-grade PMMA films onto different substrates, so it is a well-optimized technique [76]. When depositing PMMA embedded with nanoparticles, achieving an even distribution throughout the polymer matrix is crucial. Spin-coating provides excellent control over film thickness simply by varying parameters such as rotor velocity,

acceleration and time, allowing for precise control of the PMMA thickness as well as a good distribution of particles and reproduction of samples with the same properties. After the Spin-coating process, the samples need to be cured in an oven, to allow the evaporation of the solvent.

To produce the first devices the set of conditions present on Table 3, under the "Initial Conditions" line, were used based on the literature and the team know-how. During the production stage, to optimize the entire process, different parameters were used. In Table 3 all the conditions are presented, being that the modifications from the initial conditions are highlighted in grey. In the first stage (samples A and B) there was only a change in the curing temperature. In the second stage (samples 1 to 6) all the parameters were modified except for the acceleration and time of spinning. In the last stage, both velocity, acceleration and time were altered, and the curing stage was the same once it was realized that 60°C for 1 h was enough to cure the deposited layer.

Table 3 - Conditions used in the Spin-Coating and curing process.

	Samples	Spin Coating			Curing	
		Velocity (rpm)	Acceleration (rpm/s)	Time (s)	Temperature (°C)	Time (h)
ZnO	**Initial**	**1000**	**2000**	**30**	**60**	**2**
	Sample A	1000	2000	30	60	2
	Sample B				40	48
	Sample 1	500	2000	30	60	2
	Sample 2	1500				
	Sample 3	1000			40	
	Sample 4				80	
	Sample 5				60	1
	Sample 6					3
	Sample a	500	1000	30	60	1
	Sample b	1000		10		
	Sample c	500				
TiO_2	**Initial**	**1500**	**2000**	**30**	**110**	**48**
	Sample A	1500	2000	30	40	48
	Sample 1	1000	2000	30	60	2
	Sample 2	2000				
	Sample 3	1000			40	
	Sample 4				80	
	Sample 5				60	1
	Sample 6				40	20

3.2.2 Drop-Casting

Drop-casting is another commonly used method for the production of PMMA films [77]. It simply consists of dropping the solution onto the substrate (approximately 0.5 mL) and allowing it to disperse itself. However, with this technique, the thickness of the film cannot be uniformly controlled and easily reproduced. This method was used to make sure the concentration of PMMA with nanoparticles was enough to form a film, since the thickness is much higher than the spin-coated sample and to confirm some properties in the electrical characterization step.

3.2.3 Sputtering - Ion Beam Deposition (IBD)

Ion Beam Deposition (IBD) from Commonwealth Scientific was used to deposit 50 nm of tungsten as top electrode, using a metallic shadow mask to define the 300 μm in diameter circular electrodes. A base pressure of 5×10^{-7} Torr was first ensured and then a working pressure of 1.4×10^{-4} Torr under 5 sccm Argon flux, was used to pre-clean the target during 3 min and then achieve a 0.51 Å/s deposition rate.

3.3 – Characterization Methods

To gain a comprehensive understanding of the devices developed in this study, various characterization methods were employed. These methods enabled the evaluation of both the material properties and the electrical behavior of the devices. In this section, an overview of the characterization techniques used is provided, focusing on scanning electron microscopy (SEM), X-ray diffraction (XRD) and a profilometer for material properties, and electrical characterization methods for assessing the behavior of the devices.

3.3.1 Scanning Electron Microscopy (SEM)

SEM is an imaging technique used to visualize the surface of samples at a high resolution, providing information about crystal shape, surface morphology and composition of the analyzed samples. Due to its high resolution, SEM can examine aggregated nanoparticles individually, allowing the measurement of each particle. In this technique, a focused beam of electrons is scanned across the surface of the specimen. As the electrons interact with the sample, various signals are generated, which are then detected and translated into an image [78]. SEM was used in the present work to analyze the commercial nanoparticles of ZnO and TiO_2, to confirm their size and get more information on their morphology.

3.3.2 X-ray diffraction (XRD)

XRD is an analytical technique used both in single-crystal and polycrystalline materials. By exposing the sample to a beam of X-rays, its interaction with the atoms present causes constructive and destructive interference of the diffracted waves. These are captured by a detector, and through mathematical analysis, can be transformed into a diffraction pattern that reveals the unique arrangement of atoms in the crystal [78]. The resulting diffraction pattern can be presented as a diffractogram. On the y-axis is the intensity, whereas the scanning incident beam angle is displayed on the x-axis. Through the peak intensities, information about the arrangement of the crystals, the qualitative composition of the phases, and the symmetry of the space group can be retrieved. Peak shapes and widths convey information about the size of the crystallites, the presence of stacking faults, and the occurrence of antiphase

boundaries [79]. Since each compound or phase exhibits a unique diffraction pattern, specific substances within a mixture can be identified by comparing experimental patterns with established databases.

Structural characterization was performed by X-ray diffraction (Rigaku SmartLab; 45 kV and 200 mA) at room temperature using Cu-K_α radiation (1.540593 Å) and the Bragg–Brentano θ/2θ geometry in the 10°-90º 2θ range, with a step of 0.01° and scan rate of 12°min^{-1}. This method was used to study the ordering of both the embedded nanoparticles and PMMA on top of the substrate. To achieve this, the nanoparticles were placed in a Si sample holder for measurement. As for the PET-ITO substrate samples and the PMMA embedded with nanoparticles deposited on top, they were directly placed into the XRD machine to conduct the measurements.

3.3.3 Electrical Characterization

To proceed with the electrical characterization of the devices and allow for different kinds of measurements, two different devices were used. In this section, the experimental setup implemented will be presented as well as the operation modes.

A. Setup

As for the setup, two tungsten probes were connected to the top (probe itself or 50 nm tungsten thin film) and bottom (130 nm ITO thin film) electrodes. The voltage was always applied to the top electrode, whereas the bottom electrode stayed grounded. The current flowing perpendicularly between the bottom and top electrodes was then measured.

The probes were initially connected to a Keithley 2400-C SourceMeter, that applied the potential to the device as well as read the current response. The SourceMeter was used together with a homemade LabView interface, which allowed for the manipulation of all the parameters needed. In a subsequent experimental phase, another device was used to perform the measurements, the ArC One hardware platform, together with its software, from ArC Instruments [80], which allowed for better control of pulse width down to 90 ns.

Since the desired devices are meant to be flexible, all these measurements were performed both with the device in flat and bent conditions, which can be observed in Figure 11. For the flat measurements, one tip was positioned on the corner of the device, specifically where no active layer was deposited (only ITO). The other tip was placed on one of the circular electrodes (Figure 11 (A)). After testing the electrical characteristics of the device in flat mode, different bent configurations were tested, to evaluate its performance. The devices were bent at 30º [Figure 11 (B)] and at 60º [Figure 11 (C)]. During the bending, the tips were positioned similarly to the flat mode. After the bent measurements, electrical measurements were once again conducted with the device in the flat configuration.

B. Measurements

Specific measurements are commonly performed in memristive devices to characterize their resistive switching (RS) behavior. These will be presented in the sections that follow.

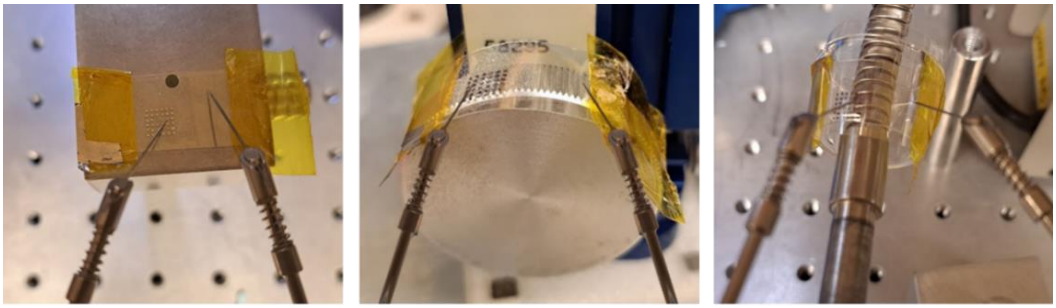

(A) (B) (C)

Figure 11 - Setup used in the electrical measurements: (A) Flat mode; (B) Bent at 30°;(C) Bent at 60°.

(i) I-V Characteristics

This measurement involves applying a ramp voltage across the device and measuring the resulting current. The I-V curve provides information about the device's resistance states, switching voltages and the magnitude of current flowing in different resistive states. With these measurements, the resistance of the device can also be monitored as a function of the stimulus, allowing for the switching behavior, including the Set, Reset and stability of each state to be determined.

The voltage sweep starts at zero, moves towards the positive potential, with a step that can be manipulated (*δV)*, returns to zero, moves towards the negative potential and, once again, returns to zero (0 V -> V_{max} -> 0 V -> V_{min} -> 0 V), as can be seen in Figure 12 (A). Asymmetrical measurements can be performed, once the voltage ramp and its step can be manipulated separately in the positive and negative ranges.

To make sure that the devices were not damaged under high current, the first measurements were performed with the Keithley Sourcemeter, once it allows the use of a lower current compliance (down to 0.001 μA), whereas Arc One can only reach 10 μA. As it was observed that the tested devices did not need a current compliance under the voltage values required to change the resistive states, the Arc One was then used as preference.

(ii) Neuromorphic Properties

Neuromorphic behavior refers to the ability of a device or system to mimic the behavior and functionalities of biological neural networks. Potentiation and depression are synaptic functions that are key aspects of learning and memory. The potential of RS devices to emulate these functions makes them susceptible to achieving an accurate mimicking of the complex dynamics of biological and neural networks, so the devices must present these properties.

Potentiation or Long-Term Potentiation (LTP), is a phenomenon observed in biological synapses where repeated activation of a synapse leads to an increase in the strength of the connection between two neurons [81]. In RS devices, potentiation refers to the ability to increase the conductance or decrease the resistance upon repeated stimulation, representing an increase in the strength of the connection between two artificial neurons or artificial synapses in a neuromorphic circuit.

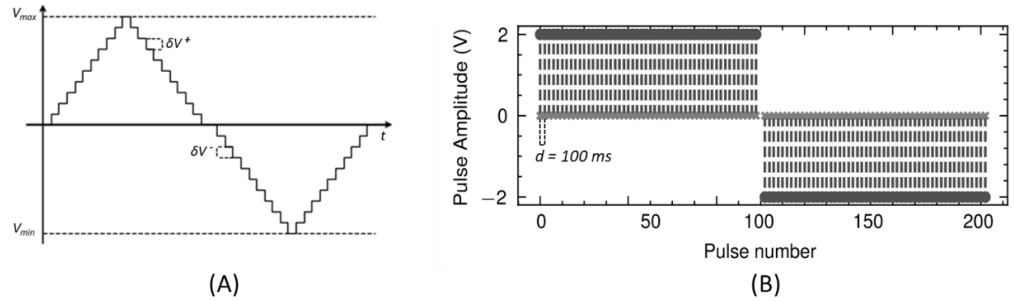

(A) (B)

Figure 12 - Schematic of the different measurement routines applied to the devices: (A) Voltage ramp for I-V Characteristics; (B) Pulses applied for evaluation of the Neuromorphic Properties.

Depression, or Long Term Depression (LTD), is the opposite of LTP, representing a weakening of the synaptic connection between two neurons due to reduced activation [81]. In RS devices, it refers to the ability to decrease the conductance upon low-frequency pulses or specific stimuli. This behavior can simulate a decrease in the strength of the connection between artificial neurons or artificial synapses.

To test these properties, an ArC One routine was used, where the device was subjected to consecutive positive and negative pulses, while its conductance was retrieved. The amplitude of the positive and negative pulses, as well as the delay between them, was manipulated. 100 consecutive positive and negative pulses were applied, with the delay between them being 10 ms, 100 ms or 200 ms. An example of the routine applied for this measurement can be observed in Figure 12 (B), where 100 2 V pulses were applied, with 100 ms of delay between them, followed by 100 -2 V, also with 100 ms of delay between each one.

(iii) Endurance

Endurance is an important characteristic of RS devices, particularly in the context of their application in non-volatile memory and neuromorphic computing. It refers to the ability of a device to withstand repeated switching cycles without significant degradation or failure [82].

Since measuring repeated I-V voltage sweeps might be a slow process, to test the endurance of the devices, consecutive positive and negative pulses, that can transit the device between resistive states, were applied. A routine from Arc One software was used to perform endurance tests, over 500 positive and negative pulses, with 10 ms of interpulse.

(iv) Retention

Retention is also a key characteristic of RS devices. It refers to the ability of the device to maintain its resistive state over time, even in the absence of external power or stimuli. When a certain resistive state is set in an RS device, it should remain stable for an extended period, ensuring reliable and persistent storage of information.

To measure it, the device was set to a resistive state with the respective pulse or voltage ramp and the resistance was measured every second for one minute. Longer measurements were also performed, where the retention was measured every second for 2 min, 5 min and 10 min.

Chapter 4

Results

The characterization of RS devices is crucial for assessing their functionality, reliability, and suitability for practical implementation. The primary focus of this chapter is to evaluate the material properties, electrical characteristics, and performance of the RS devices, through the analysis of the obtained results, allowing a deeper understanding of the devices fabricated.

4.1 – Material Properties

This section will focus on examining the material properties of the resistive switching layers. Structural analysis techniques such as SEM, XRD were employed to investigate the crystalline structure, size of the nanoparticles, material composition and ordering. In addition to the techniques mentioned, a Leica optical microscope was also employed to further examine the samples and provide a better understanding of their surface. Moreover, a regular smartphone camera was employed to capture visual images for qualitative analysis of the samples' physical appearance.

4.1.1 Nanoparticles Size

In this study, SEM was used to confirm the size of the nanoparticles of ZnO and TiO_2 used as well as get more information on their morphology. Figure 13 shows representative SEM images of the nanoparticles used, highlighting their size and morphology. Figure 13 (A) shows that the TiO_2 (30 nm) nanopowder exhibits a relatively uniform size distribution of the particles, ranging from 24.88 nm to 43.27 nm, with a mean of 33.56 nm and a standard deviation of 6.12 nm. Figure 13 (B) shows that the TiO_2 nanopowder of 100 nm, has a lower mean, of only 64 nm, with particles from 49.20 nm to 75.21 nm, smaller than expected. When it comes to Figure 13 (C), SEM image of the ZnO (100 nm) nanopowder, the nanoparticles present a uniform size between them, but with a deviation higher than the TiO_2, with the particles sizes ranging from 63.21 nm to 163.5 nm, with a mean of 114,14 nm and a standard deviation of 39.11. In all the powders, the nanoparticles appear to have a spherical or near-spherical shape, indicating their well-defined structure, allowing for precise size control, uniformity, and efficient charge transport, all of which contribute to reliable and predictable resistive switching behavior.

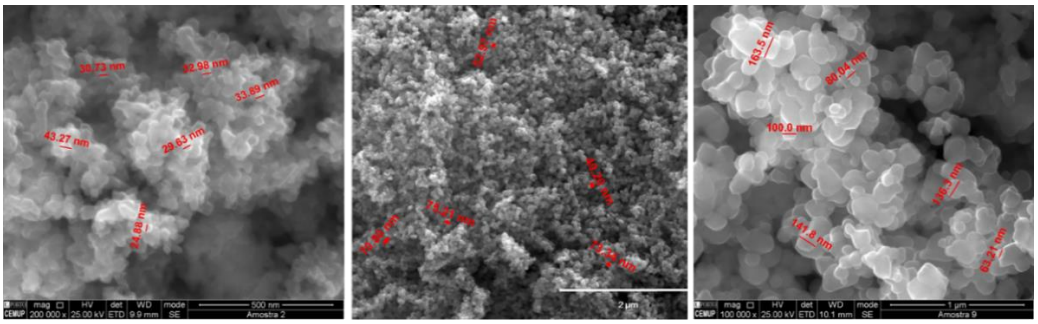

Figure 13 - SEM images of the nanopowders used for the fabrication of the devices: (A) TiO_2 30 nm; (B) TiO_2 100 nm; (C) ZnO 100 nm.

4.1.2 Crystalline Structure

In this work, XRD was used to study the ordering of both the embedded nanoparticles and PMMA on top of the substrate, comparing the results with literature diffraction patterns as well as the XRD of the nanoparticles. Figure 14 displays the diffractograms of the 100 nm nanoparticles of ZnO and TiO_2 along with their diffraction patterns when embedded in PMMA on top of the PET-ITO substrate, specifically with a composition of 60% ZnO for Figure 14 (A) and 11% TiO_2 for Figure 14 (B). Additionally, both figures show the diffractogram of the PET-ITO alone. Vertical lines in the diagrams represent the literature diffraction patterns of the different materials, aiding in the analysis of peak orientation.

When it comes to the XRD analysis of the ZnO and TiO_2 nanoparticles, the diffraction peaks obtained match well with the literature diffraction patterns. These peaks are clearly visible and indicate the presence of the respective nanoparticles.

When examining the XRD pattern of the PMMA embedded with ZnO on the PET/ITO substrate, all the peaks from both the substrate and ZnO can be observed. However, the peaks corresponding to the ZnO nanoparticles are less prominent. Nonetheless, they are still discernible, indicating the presence of embedded ZnO within the PMMA matrix.

In contrast, for the XRD pattern of the PMMA embedded with TiO_2 on top of the PET/ITO substrate, the peaks associated with TiO_2 are not as prominent. The intensities of these peaks are noticeably smaller and mostly coincide with the peaks originating from the PET/ITO substrate. This suggests that the presence of TiO_2 within the PMMA matrix is not as pronounced or has a lower concentration compared to the other materials, which is expectable once its concentration in the PMMA is only 11%.

Considering PMMA's typical amorphous behavior, it does not exhibit well-defined peaks in XRD analysis, so its presence cannot be proved with this technique.

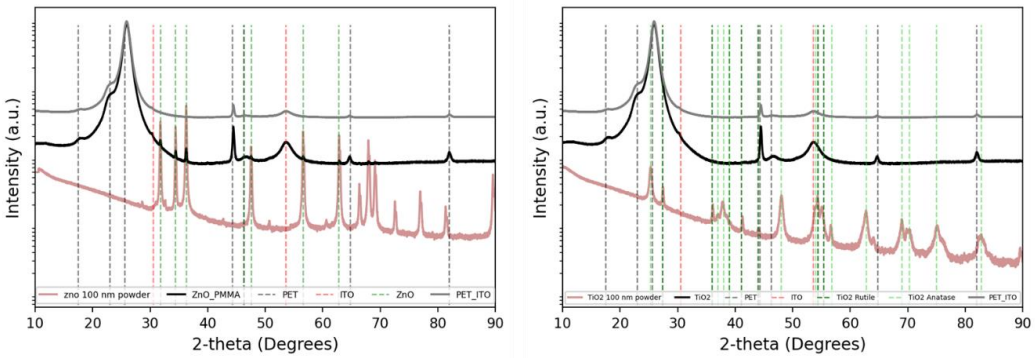

(A) (B)

Figure 14 - XRD patterns of the nanoparticles alone and embedded in the PMMA deposited on top of PET/ITO. The vertical lines represent the literature indexed peaks of the different materials: (A) PET/ITO in grey, ZnO embedded in the PMMA in black and ZnO 100 nm nanoparticles in brown; (B) PET/ITO in grey, TiO_2 embedded in the PMMA in black and TiO_2 100 nm nanoparticles in brown.

4.1.3 Layer thickness

A Bruker Dektak XT profilometer with 1 stylus force over a 500 μm range (15 μm/s) was used to calibrate the thickness of the spin coated layers. A thickness of around 400±10 nm was obtained for a layer deposited under 1000 rpm for 10 s, as expected from the literature [83].

4.1.4 Device's architecture

An optical microscope was used to obtain a detailed examination of the device's surface. Although the nanoparticles (ZnO and TiO_2) were roughly the same size 100 nm, the TiO_2 ones appeared to be a bit smaller (with a mean of only 64 nm, when compared to 114 nm from the ZnO), as observed in the SEM images from Figure 13. The samples were produced with the same concentration of nanoparticles in the PMMA (11 %), same curing time (60º C for 1h), but slightly different spin-coating parameters. The sample embedded with ZnO was deposited at 500 rpm for 30 s, with 1000 rpm/s of acceleration, whereas for the TiO_2 one, the velocity was 1000 rpm, spin-coated for 10 s at 2000 rpm/s of acceleration. On top of both samples were deposited the W circular electrodes by sputtering. In Figure 15 both samples are represented through the optical images obtained. In Figure 15 (A) and (C) can be seen the interface of the substrate (PET/ITO) and the deposited layer on top, of PMMA with ZnO or TiO_2, respectively. Like it was observed at the naked eye, the ZnO sample presented a better distribution of nanoparticles when compared to the TiO_2 one, which is now clearer with these images. This might have happened due to the differences in the spin-coating parameters or the different affinity that the nanoparticles might have with the PMMA. Figure 15 (B) and (D) show the deposited circular electrodes. As these images were acquired after the electrical measurements, some damage can be seen in some of the electrodes, as it is the case of the one on the left corner of Figure 15 (D), in which the entire layer of both the electrode and the PMMA were removed.

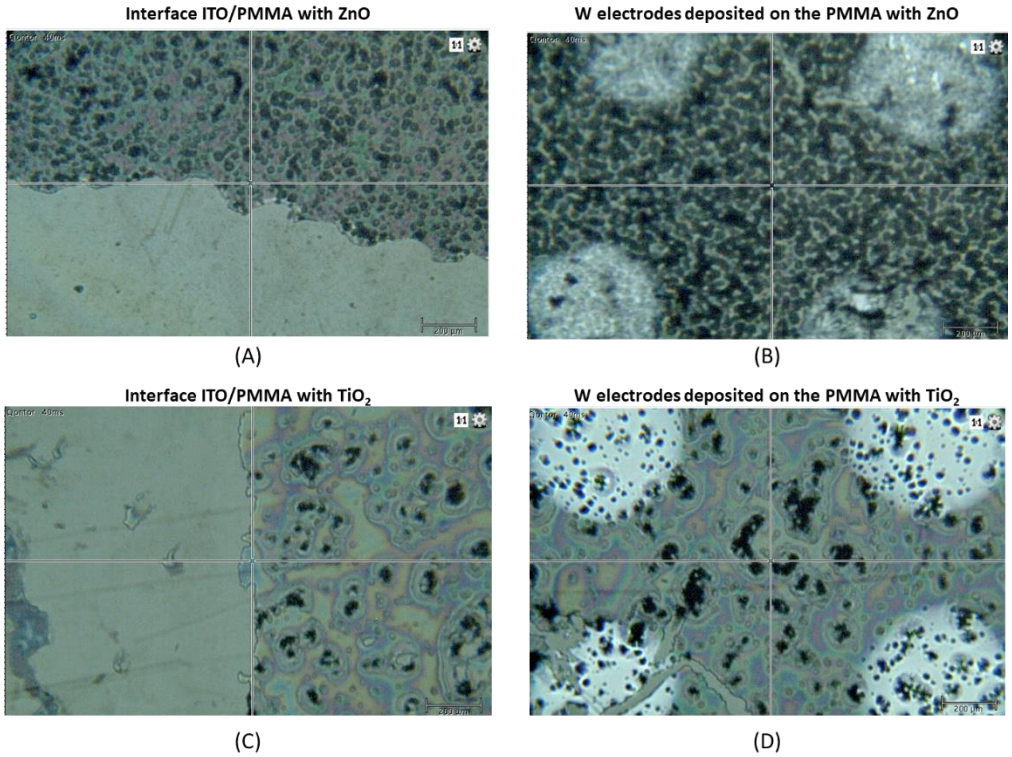

Figure 15 - Optical images of the final samples under 5x magnification: (A) Interface between the substrate of PET/ITO and the PMMA embedded with ZnO (11%) deposited on top; (B) Tungsten (W) electrodes deposited on top of the PMMA+ ZnO layer represented on (A); (C) Interface between the substrate of PET/ITO and the PMMA embedded with TiO_2 (11%) deposited on top; (D) Tungsten (W) electrodes deposited on top of the PMMA+ TiO_2 layer represented on (C).

Some pictures of the final devices (11% of ZnO or TiO_2) were taken with a regular smartphone camera to illustrate its characteristics.

In Figure 16 (A) is represented the ZnO device in a flat configuration. As can be seen it presents a very small thickness and is very transparent. In Figure 16 (B) and (C) is presented the TiO_2 folded with the substrate of PET inwards and outwards, respectively. The flexible character of the device is clearly seen here. Moreover, the deposited W electrodes can be distinguished, as well as the interface between where the PMMA was deposited and the ITO.

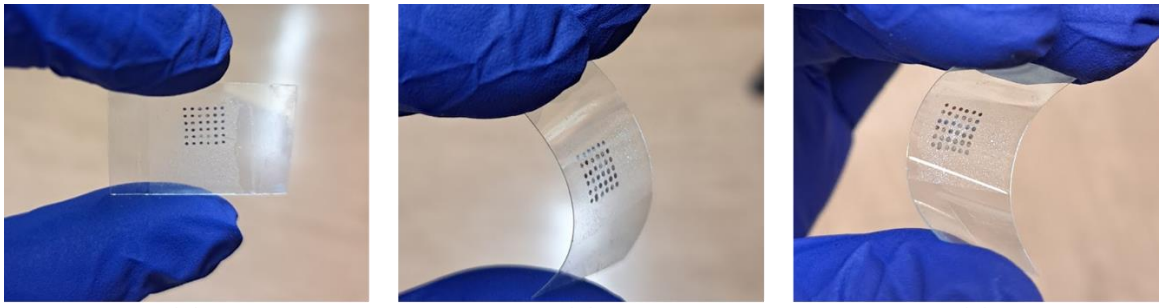

Figure 16 - Pictures of the final devices: (A) ZnO flat; (B) TiO_2 folded one way (with the PET inside the curvature) and another (with the PET outside the curvature).

4.2 – Electrical Properties

This section is dedicated to exploring the electrical characteristics and performance of the system through a range of measurements, which plays a vital role in understanding the behavior and functionality of the devices.

4.2.1 I-V Characteristics

A. Different Spin-Coating parameters

The I-V behavior of the devices was evaluated with the probe as the top electrode and different voltage ramps were applied (namely 1/-1 V, 1.5/-1.5 V and 2/-2 V), with δV of 0.05 V.

In Figure 17 are represented the I-V curves from samples with 3 different spin-coating conditions, when it comes to their spinning velocity and time, namely 500 and 100 rpm, for 10 or 30 seconds, with V_{max}= 2 V and V_{min}= -2 V. When applying a positive bias, from 0 V to V_{max} to 0 V all the samples performed RESET, which means their resistance increased, going from a LRS to a HRS. When the opposite bias was applied (0 V ->V_{min} -> 0 V) a SET was observed, that is, the resistance decreased, leaving the device in a LRS.

Both the 500 rpm device spun for 10 seconds, and the 1000 rpm spun for 30 seconds, showed similar behavior, with a difference in the switch in the $10^2\,\Omega$ order of magnitude, and a ratio of around 1.6. The higher switches occurred in the 1000 rpm sample spun for 10 seconds with a difference of $2x10^3\Omega$ (ratio = 2.77), and 500 rpm spun for 30 seconds of $10^3\,\Omega$ (ratio = 2.50), being that the latest presented the most gradual transitions.

The sample spun at 500 rpm for 30 s showed the most pronounced resistance transition, which may be explained by a thicker layer compared to the 1000 rpm. However, regarding the 10 s vs the 30 s results, further studies are needed to understand this influence.

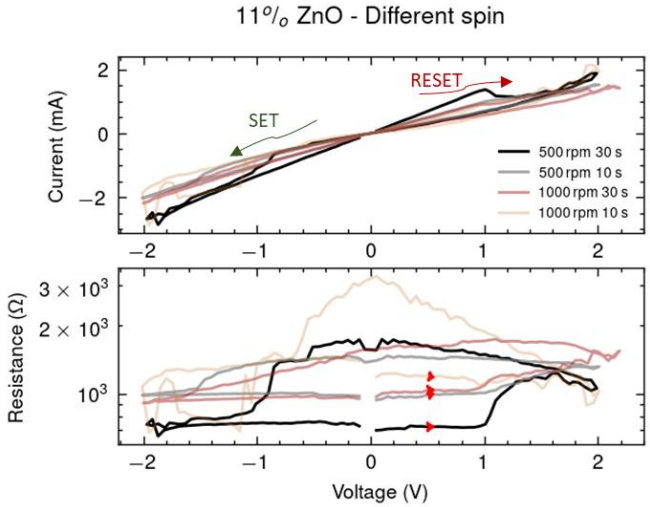

Figure 17 - I-V curves comparing the influence of the spin-coating parameters in samples with 11% of ZnO.

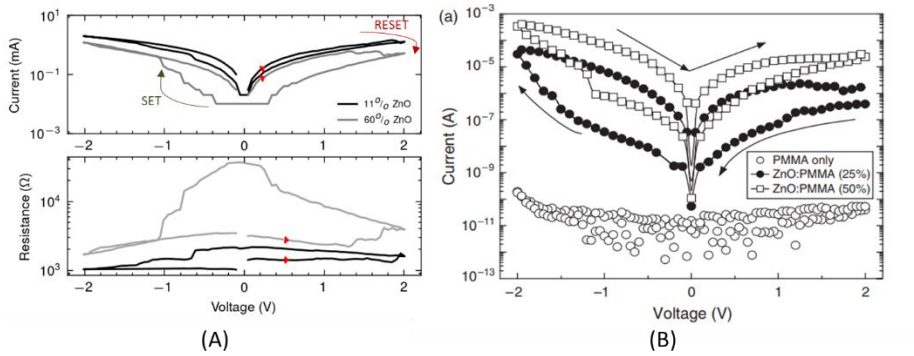

Figure 18 - I-V curves comparing the behavior of devices with different concentrations of ZnO, with the current in logarithmic scale: (A) results obtained from this work at ZnO concentrations of 11% vs 60%, with Vmax= 2 V, Vmin= -2 V; (B) Behavior of similar devices comparing different concentrations of ZnO - 25% vs 50% provided from [57]**.**

B. Different concentrations

This section presents the comparison of the I-V behavior of the devices with different concentrations of nanoparticles, using the probe as the top electrode. As it will be demonstrated, independently the concentration of the nanoparticles, all devices showed RS behavior, from voltages ramps of 1/-1 V, 1.5/-1.5 V and 2/-2 V. With the positive ramp, they switch to a higher resistive state (RESET), whereas with a negative one, they switch to a lower resistive state (SET).

(i) 11% vs 60% ZnO

As can be observed in Figure 18 (A), the devices with both concentrations of the nanoparticles showed resistive switching behavior. For the 11% of ZnO the switch is from ≈1.4 kΩ to ≈2.4 kΩ (a difference of ≈1 kΩ, ratio = 1.75) and the 60% of ZnO from ≈3.1 kΩ to ≈32.7 kΩ (a difference of ≈30 kΩ, ratio = 10^1). This means that an increase in concentration leads to a higher distinction between the two resistive states. Looking at the shape of the hysteresis, the higher concentration device also presents a less abrupt switching behavior, which is usually helpful in the control of the neuromorphic behavior. Furthermore, a decrease in the current response when increasing the concentration of the ZnO nanoparticles (from 11% to 60%) is observed. This is not in total agreement with other works [Figure 18 (B)], that studied a film of PMMA with 25% and 50% ZnO of around 70 nm [57]. A difference in the thicknesses might explain the decrease in current, as well as a saturation effect above 50% (our case). Note that the PMMA deposited on top of the ITO without nanoparticles was also measured and did not show RS, so it is not shown.

Looking at the aspect of the samples, the one with higher concentration of nanoparticles had more “blank spaces”, that clearly had no nanoparticles. This might be explained because in higher concentrations of nanoparticles aggregation is exacerbated, primarily driven by van der Waals forces. Consequently, the particles tend to aggregate, leaving more areas occupied solely by the PMMA matrix, that does not present RS behavior. The resulting large clusters not only made it harder to measure the samples, but also made the switching layer more susceptible to damage during measurements, leading to compromised results. These were aggravated upon bent measurements, in

which the 60% sample showed worst results, mostly because it was harder to place the probes in a location where there were nanoparticles and more damaged was being made upon measurements.

Comparing both, although the increase in concentration improves the RS behavior of the device when flat, due to the higher aggregation of the nanoparticles, this behavior is worse in bent measurements.

(ii) 11% vs 20% TiO2

The same response was obtained in the TiO_2 devices produced with different concentrations, the current was lower in the higher concentration sample, however with a smaller discrepancy, when compared to the ZnO devices. The curves obtained were very similar to the ones belonging to ZnO in Figure 18. Once again in the higher concentration sample, there was a bigger aggregation of the particles, leading to the same aggregation problems mentioned.

C. Different Nanoparticles Size

This section presents the comparison of the I-V behavior of the devices with the same concentration of nanoparticles with different sizes, namely 11% of TiO_2 embedded in the PMMA, with 100 nm and 30 nm in diameter, using the probe as the top electrode.

It is shown in Figure 19, that the 30 nm nanoparticles [Figure 19 (C)] tend to aggregate more than the 100 nm ones [Figure 19 (B)]. This might have happened because smaller particles tend to have a higher packing efficiency, allowing them to be closer together in the PMMA matrix. On the other hand, larger particles may require more space, resulting in a larger separation between each other.

Regarding their I-V behavior, their curves are of similar format and a SET is performed with a negative voltage and RESET with a positive one. However, when looking at the resistances, the 100 nm device switches from ≈2 kΩ to ≈32 kΩ, which is a difference of $3x10^4$ Ω (ratio = 16), one order of magnitude higher than the switch performed by the 30 nm one and with a ratio eight times higher (from ≈4 kΩ to ≈8 kΩ, which is a difference of $4x10^3$Ω, ratio = 2). Also, since for 30 nm the particles were closer together, it was more probable to only be measuring the PMMA. Folded measurements were harder to perform on the 30 nm sample. This makes the 100 nm particles more advantageous to the production of the devices.

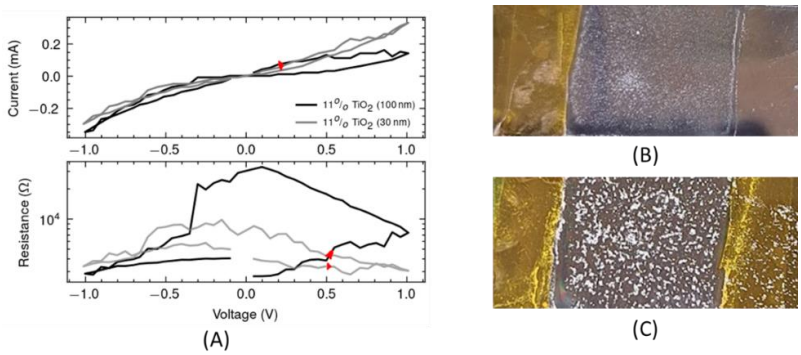

Figure 19 – Effect of the size of the TiO_2 nanoparticles: (A) I-V curves of the devices produced with 11% of TiO_2 with 100 nm and 30 nm, with Vmax= 2 V, Vmin= -2 V; (B) Image of the sample with TiO_2 with 100 nm; (C) Image of the sample with TiO_2 with 30 nm.

D. Effect of the circular electrodes

We further compare the I-V behavior of the devices when a W thin film is deposited on as top electrode to when only the W probe is used.

The behavior of the ZnO device remained consistent with and without the electrode under the same measurement conditions (δV = 0.05 V, Vmax = 2 V, and Vmin = -2 V) when the device was in a flat state, as shown in Figure 20 (A). After a few measurements with the device folded at 30º, the electrode and the active layer were damaged, leading to the presentation of curves characteristic of the ITO. A similar effect was observed when the electrode was not deposited. Figure 20 (B) and (C) illustrate the behavior of the devices without and with the W electrode, respectively, along with the curves obtained by measuring solely on the ITO. It can be observed that the curves are similar in both shape and range, however it is to take note that the sample with the electrode depicted very small currents, close to the equipment resolution, leading to there being more noise. This observation suggests that the active layer and the electrode were damaged by the tip during the measurements, and the voltage ramp and I-V response was applied and coming from the ITO layer. Note that the RS behavior changes, with SET taking place at positive voltage and RESET at negative.

The same behavior happened in the TiO_2 device, although the electrodes made the device more robust, especially when folded, allowing to improve the measurements.

E. ZnO or TiO_2 embedded in PMMA with Tungsten (W) circular electrodes

In this section will be presented the I-V characteristics of the two optimized final devices fabricated in this work. The devices consist of a layer of PMMA embedded with nanoparticles (ZnO or TiO_2, both at 11%) deposited on top of a PET/ITO sheet, with circular W electrodes deposited on them. These can be observed in Figure 16.

Different voltage ramps were applied for both devices, with a voltage step (∂V) of 0.05 V, while remaining flat and bent (at 30º and 60º). Both devices showed two different states, a high and a low resistive state, that were achieved through different voltage ramps, namely (V_{max} = 2 V, V_{min} = -2 V), (V_{max} = 1.5 V, V_{min} = -1.5 V) and (V_{max} = 1.5 V, V_{min} = -1 V).

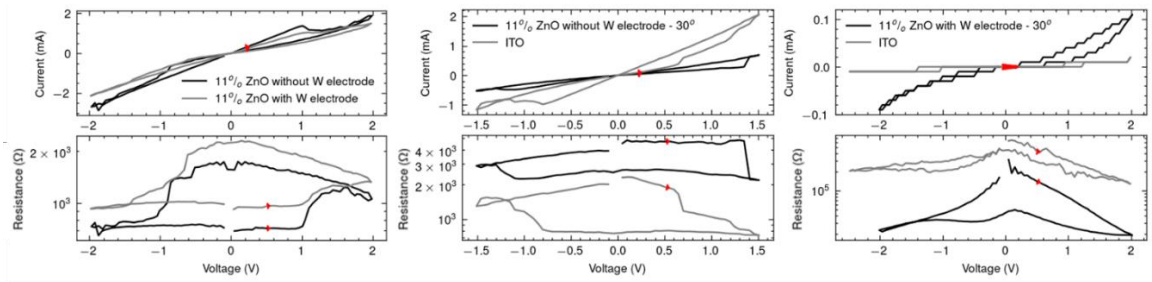

(A) (B) (C)

Figure 20 - I-V curves comparing the behavior of ZnO devices with W electrode and probe as top electrode:(A) Flat with Vmax = 2 V, Vmin = -2 V; (B) Comparison between the device without the electrode, at 30º with Vmax = 1.5 V, Vmin = -1.5 V and the ITO I-V response with the same parameters; (C) Comparison between the device with the electrode, at 30º with Vmax = 2 V, Vmin = -2 V and the ITO I-V response with the same parameters.

Throughout the measurements it was observed that their behavior was stochastic, meaning that with the same exact conditions they presented different current and resistive responses, as it is typical in these types of devices. However, all of them presented curves that indicate that their switching is bipolar, once that the V_{SET} is smaller than V_{RESET}. Also, with a positive voltage ramp they switch to a higher resistive state (RESET) and with a negative voltage ramp they return to the low resistive state (SET), and the best results were obtained with (V_{max} = 2 V, V_{min} = -2 V).

The I-V performance of the devices under different conditions is illustrated in Figure 21. In Figure 21 (A) are represented the I-V curves obtained for the ZnO device in the three configurations, flat, bent at 30º and at 60º in a different electrode, with (V_{max} = 2 V, V_{min} = -2 V). Similarly, in Figure 21 (B) are represented the I-V curves obtained for the TiO_2 device in the same three configurations, for the same voltage ramps.

Comparing the performance in both devices flat, the TiO_2 device had a higher switch, going from a lower resistive state (≈353 Ω compared to ≈926 Ω from the ZnO), to a higher one (≈4224 Ω and ≈2295 Ω from ZnO), leading to the current response being almost double compared to the ZnO device.

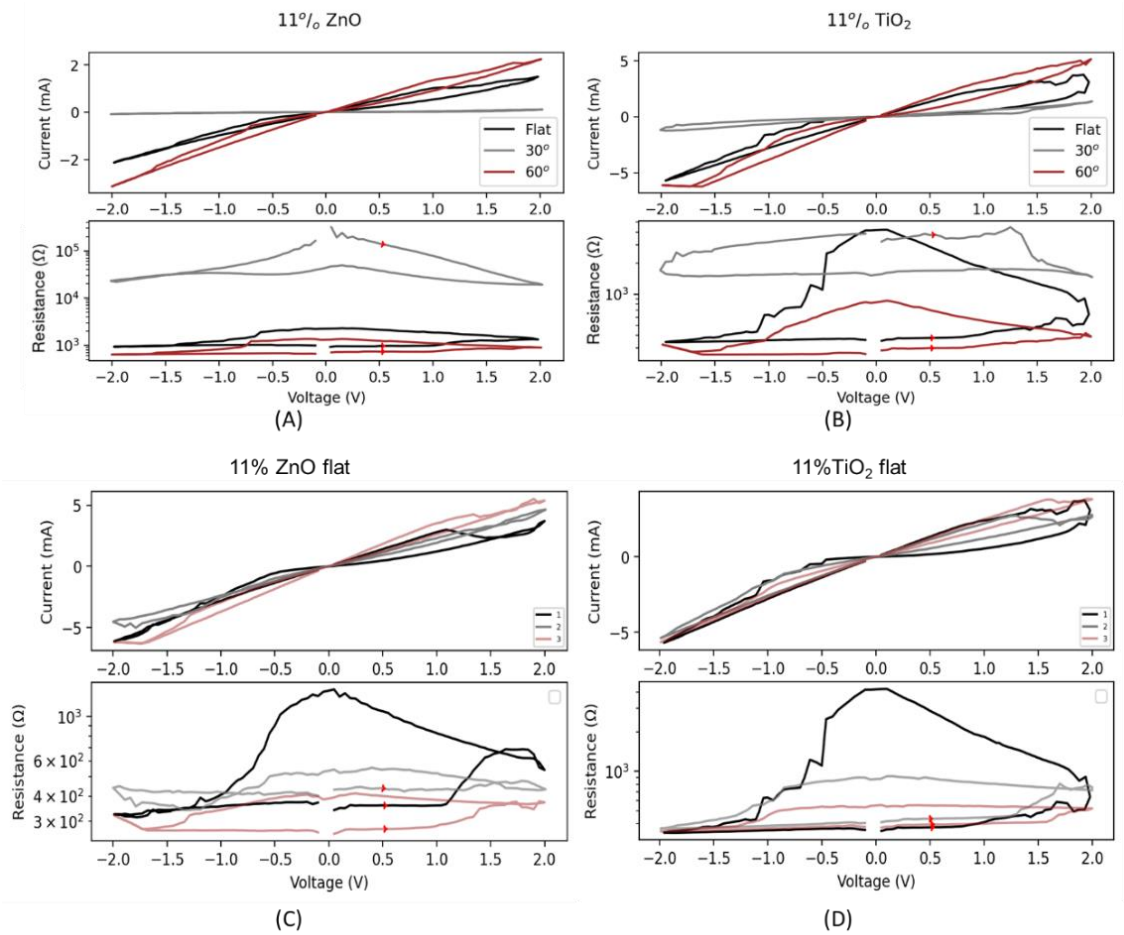

Figure 21 - I-V curves comparing the behavior of the final devices, of PMMA and nanoparticles (11% of ZnO or TiO_2) with W electrodes deposited on top, as well as the representation of the resistance in function of the voltage (Vmax = 2 V, Vmin= -2 V).The red arrow represents the direction of the resistance in the R-V curves: Flat, 30º and 60º (A) ZnO; (B) TiO_2; Flat 3 consecutive cycles (C) ZnO; (D) TiO_2.

Folding the devices at 30º and performing measurements in the same electrode, it was observed that it started to get damaged, and the I-V curves obtained started to invert, meaning that with a positive voltage ramp they switch to a lower resistive state (SET) and with a negative voltage ramp they return to the high resistive state (RESET), as can be seen in both figures in grey. After a few tests this was proved to be the curves obtained measuring on the undeposited ITO, which means that both the PMMA + nanoparticles layer, as well as the electrode were entirely removed with the probe upon repetitive measurements. This can be observed in Figure 15 (D), in the electrode in the left lower corner. Although in different ranges, the behavior in both devices folded at 30º was similar, with a resistance ratio of around 3.

Changing electrodes, a few more measurements were performed, especially at 60º. Still preserving their VCM resistive switching, the resistance in both devices and their switching interval between states lowered, when compared to the same conditions measuring the device flat.

As for each device, it seems that the folding arrangement increases the current, maybe because with the folding, the deposited layer becomes thinner. In this case, the 30º fold triggered a decrease in the current, due to the measurements being performed on the ITO layer.

In the ZnO device, the flat and bent at 60º configuration resulted in a similar switch, with a difference of around 1 kΩ and a ratio of 2.5, going from (≈926 Ω to ≈2.3 kΩ and ≈707 Ω to ≈1.8 kΩ). In the TiO_2 device, the flat measurement resulted in a switch higher than both the fold measurements, with a difference of resistive states of almost 4 kΩ, ratio = 12. As for the 60º configuration, the switch was smaller with only a difference of around 600 Ω (≈284 Ω to ≈864 Ω) and a ratio of 3.

A few consecutive measurements were also performed on the devices flat, with the same electrical parameters, (V_{max} = 2 V, V_{min} = -2 V) and δV= 0.05 V. In Figure 21 (C) and (D) are depicted the 3 consecutive measurements on the ZnO and TiO_2 devices, respectively. As can be seen, with each consecutive measurement, the current increases in both devices, being than in the ZnO the increase is more noticeable of around 1 mA between measurements. In the TiO_2 device, although the current before the RESET is similar, as soon it occurs, a difference of around 1 mA is also noted between measurements. When it comes to the resistance switch between states, it is clear that the first measurement has the highest ratio (4 Ω for ZnO and 12 Ω for TiO_2). The ratio between states in the TiO_2 device declines with the measurements. From the first to the second measurement there is an 82% decrease, whereas the second to the third, there is a 36% decrease, but with the LRS similar between samples. In the ZnO device, the LRS decreases with the three measurements. From the 1st to the 2nd there is a 70% decrease in the ratio between resistive states, whereas from the 2nd to the 3rd there is a 25% increase.

4.2.2 Endurance

In this chapter will be presented the characterization of the devices when it comes to their endurance.

A. ZnO or TiO_2 embedded in PMMA with Tungsten (W) circular electrodes

To characterize the endurance of the devices is to analyze whether they can withstand repeated switching cycles without significant degradation or failure.

In Figure 22 is represented the behavior of the devices upon 1000 consecutive positive and negative pulses (with 10 ms interpulse), capable of switching the device between resistive states (2 V and -2 V). Once again, these measurements were performed with the devices flat, bent at 30º and 60º.

Comparing the results in the flat devices it is clear that the ZnO device, although presenting a lower conductance gap than the TiO_2 (0.1 mS for the ZnO and 1 mS for the TiO_2), could maintain its conductance state over the course of the measurement, with more stability. However, when folded at 30º, the switching between states was very low (0.0001 mS), probably not due to the folding itself, but due to the damaging of the top electrode during the measurements. This measurement was repeated in different electrodes, but although they showed RS, the endurance behavior was similar to the presented. For 60º fold, there is a decrease in the resistance gap, with the ON conductance slightly decreasing and the OFF increasing.

Both the 30º and the 60º folds in the TiO_2 device have improved performance when it comes to the endurance, with the conductance gap increasing approximately 0.1 mS from flat to 30º and 30º to 60º, being that the latter shows more stability, while both flat and bent at 30º configurations suffer alterations in the first 300 cycles, before stabilizing. Interestingly, the ZnO devices presents better endurance when flat, whereas the TiO_2 endurance seems better when folded. This might happen because the active layer might become thinner in folded measurements, and this can be favorable in terms of endurance for the TiO_2 device.

In terms of endurance, some results were observed in other samples produced with different conditions, but the final devices presented better performance.

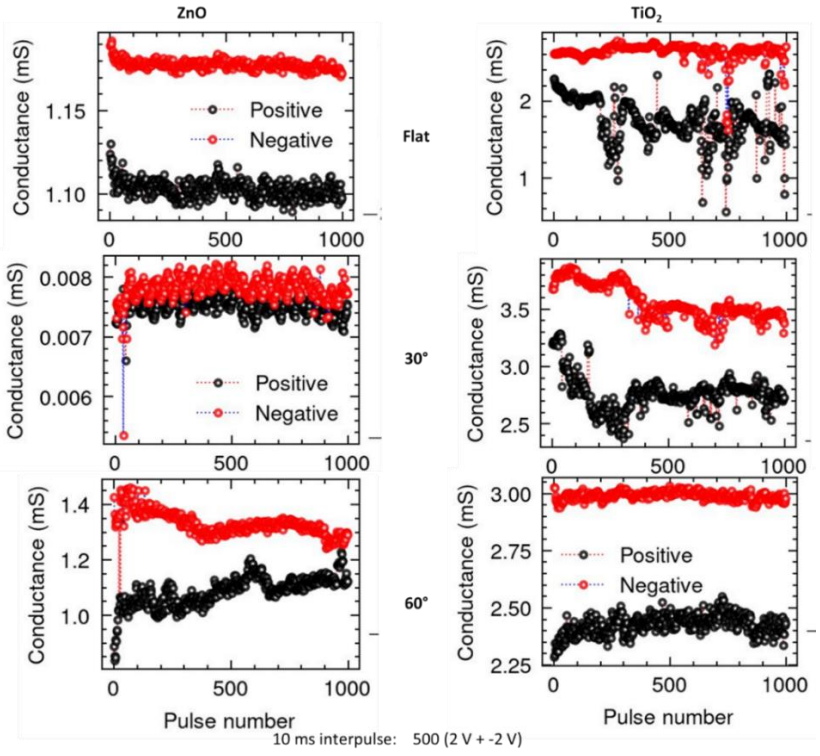

Figure 22 - Endurance of the two final samples, 11% of ZnO or TiO_2. Retrieved conductance while applying 1000 consecutive pulses of 2 V and -2 V with an interpulse of 10 ms. Measurements performed with the devices flat, bent at 30º and 60º.

4.2.3 Retention

In this chapter will be presented the characterization of the devices when it comes to their retention.

A. ZnO or TiO_2 embedded in PMMA with Tungsten (W) circular electrodes

The retention of the devices is evaluated by their capacity to maintain a certain resistive state for a period. In Figure 23 is represented the behavior of the devices after being placed in a HRS with a SET pulse or voltage ramp, where their resistance was measured every second for a period, with a reading pulse of 0.5 V represented by the black line in each plot. The devices were then set to a LRS and once again their resistance was measured every second (red line). These measurements were performed with the devices flat, bent at 30º and 60º.

When both devices were flat, their retention was satisfactory, showing a clear separation between the two states over 5 and 10 min for ZnO and TiO_2, respectively. For ZnO some fluctuations of the ON state were observed after 5 min and the TiO_2 device shows a slightly higher gap between the resistive states, as the conductance goes from ≈0.5 mS to from ≈1.5 mS (Δ≈1 mS), whereas in the ZnO it goes from ≈0.6 mS to from ≈0.95 mS (Δ≈0.35 mS).

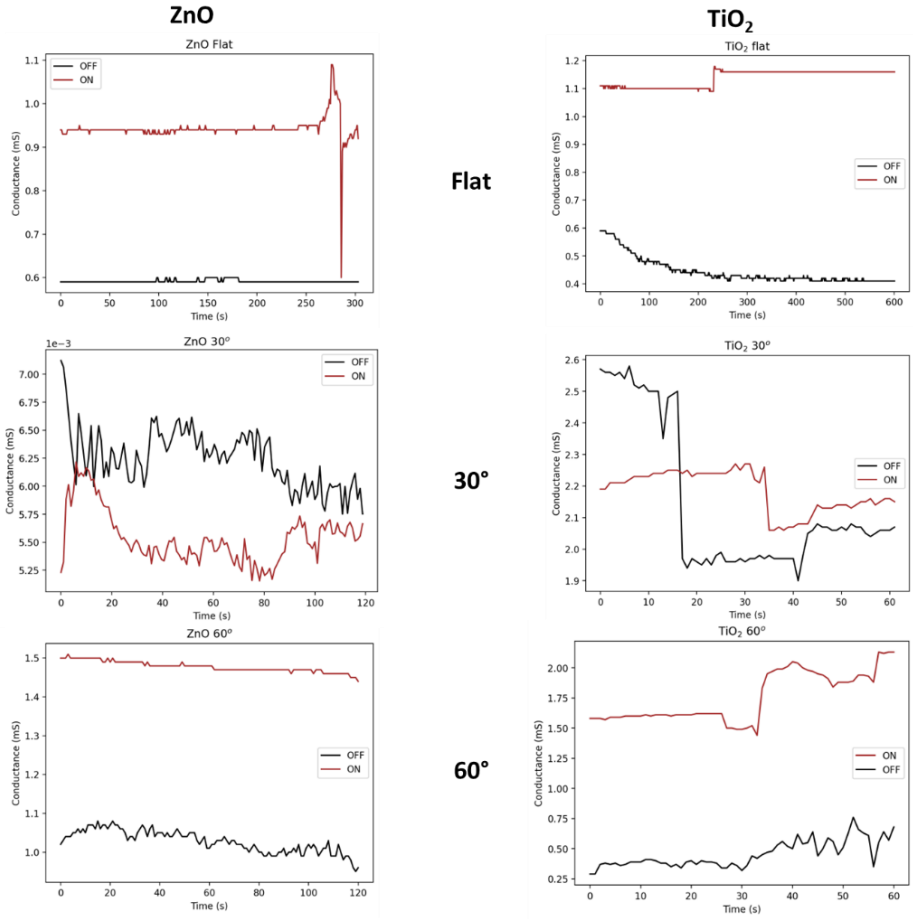

Figure 23 – Retention of the two final samples, 11% of ZnO or TiO_2. Conductance read for different amounts of time, every second, after putting the device in HRS (OFF) and LRS (ON). Measurements performed with the devices flat, bent at 30º and 60º.

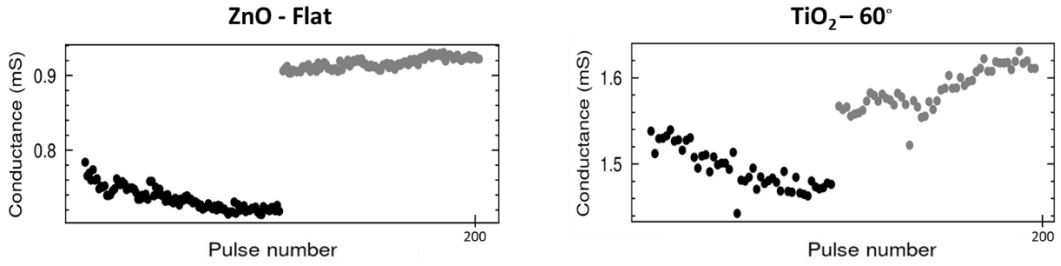

Figure 24 - Neuromorphic behavior of the two final samples, 11% of ZnO (flat) and TiO_2 (folded at 60°). Retrieved conductance while applying 100 pulses of 2 V and -2 V with an interpulse of 100 ms.

When folded at 30° an unusual behavior is observed for both cases, with the OFF conductance even seeming to be higher than the ON conductance. As this is unreasonable, the most likely explanation is that the measurements were performed on the ITO layer. This explains why after a positive voltage the conductance is high instead of low and why it is low after a negative voltage [see Figure 20 (B)]. When the measurements were performed at 60°, the retention of the devices seemed to improve compared to the previous fold. The ZnO device was able to maintain its retention for a longer time (2 min), whereas the TiO_2, started to present some changes after 30 s, with both resistive states lowering after this period. Also, for these measurements the difference between resistive states was even higher, when compared to the flat configuration ($\Delta TiO_2 \approx 1.3$ mS and $\Delta ZnO \approx 0.5$ mS). These results show that the PMMA with nanoparticles has non-volatile RS behavior when flat and folded since both devices are able to maintain their resistive state in the different configurations.

B. Effect of the other parameters

The effect of the W deposited electrodes, different concentration of the nanoparticles in the PMMA, their size and different spin-coating parameters did not seem to make much of a difference when it comes to the retentions of the different devices.

4.2.4 Neuromorphic Properties

In this chapter will be presented the characterization of the devices when it comes to their neuromorphic properties.

A. ZnO or TiO_2 embedded in PMMA with Tungsten (W) circular electrodes

To analyze the neuromorphic behavior of the devices, their ability to present depression (decrease in the conductance, LTD) and potentiation (increase in the conductance, LTP) must be considered.

In Figure 24 is represented the behavior of the devices upon 100 positive and 100 negative pulses, capable of transitioning the devices between resistive states (2 V and -2 V). These measurements were performed while the devices were flat, bent at 30° and 60°, and varying the interpulse between 10 ms, 100 ms and 200 ms.

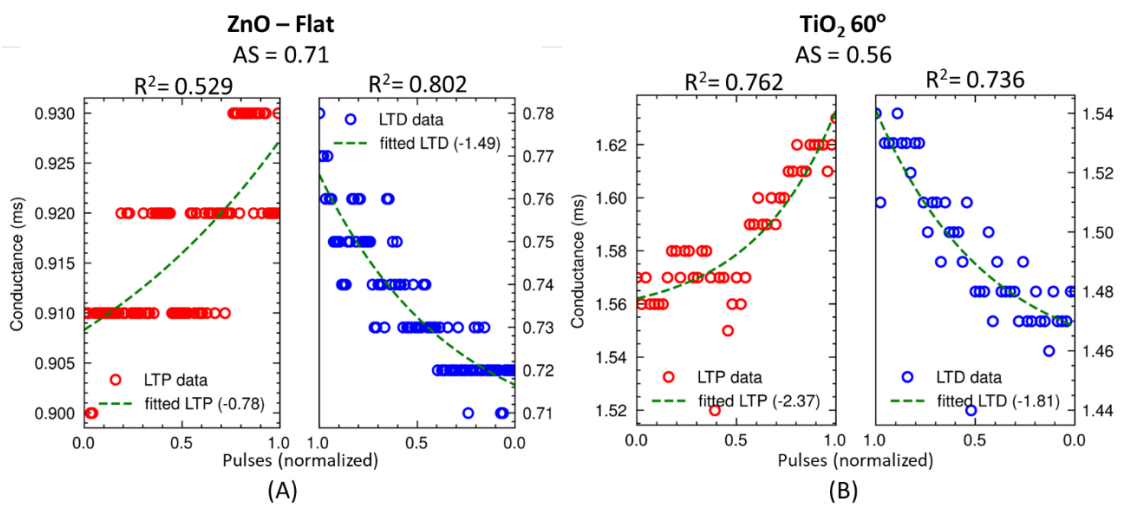

Figure 25 – Non-linearity curves obtained for the ZnO and TiO_2 final samples, together with the fitted curve. Values of AS and R^2 are also discriminated: (A) ZnO flat; (B) TiO_2 60° fold.

The best results were chosen to be presented, namely ZnO flat and TiO_2 bent at 60°, with 100 ms of interpulse. It was expected that with the positive pulses the devices presented LTD and with the negative pulses, LTP. Upon examining the results, it becomes evident that both performed accordingly, presenting LTD and LTP. An evident shift towards a higher conductive state as soon as a negative pulse (SET) is applied is also clearly observed.

A further analysis was performed to determine the Asymmetry (AS) of the curves and their coefficient of determination (R^2). AS was calculated through the difference of Non-Linearity (NL) of each of the curves (LTP and LDP), extracted through the WebPlotDigitalizer [84]. For learning applications in neuromorphic devices, AS should be inferior to 1, and as close to 0 [85]. R^2 is as close to one as the data points fit the fitted line, so this should also be taken into account. These results are presented in Figure 25. In both situations, an apparent LTP and LTD are noted. When looking into the other parameters, the best results were obtained by the TiO_2 sample, when folded at 60° [Figure 25 (B)]. AS is inferior to one and closer to zero when compared to the ZnO sample [Figure 25 (A)] and shows a better fit to the line (R^2 values are both closer to one).

Considering all these situations it can be said that both samples show promising results for this matter, by showing clear LTP and LDP and good values of AS, which are crucial aspects of the learning process.

Chapter 5

Conclusions and outlook

The research presented in this work highlights the potential of flexible resistive switching devices as a breakthrough in future implantable neuro devices. By addressing the limitations of rigid devices, these flexible devices offer improved interface and adaptability to the soft tissues of the human body.

The traditional von Neumann computing architecture, with separated memory and processing units, faces challenges due to increasing data size, resulting in energy and time inefficiencies. Memristors, a novel device class with resistive switching, offer a solution inspired by the brain's functioning, where memory integrates data storage and processing. This eliminates data movement issues between separate units and mimics synaptic behavior, once their switching behavior between two or more states of resistivity resembles synapses. These characteristics make memristors ideal for the novel neuromorphic computing architecture, as well as a great option to be used in implantable neuro devices. On the other hand, the rigidity of existing implantable devices pose challenges for interface and adaptability in the soft, high-water content tissues of the human body.

Combining the memristors capabilities to mimic the human functioning and the lack of implantable devices able to accommodate to the human body, here a solution is presented as a contender to combine these two topics and create a flexible resistive switching device, capable of being used for neuromorphic applications, such as nonvolatile memories and artificial neuromorphic arrays for wearable and implantable devices.

The device stacks were fabricated using scalable spin-coating and sputtering techniques. The active layer consists of PMMA embedded with TiO_2 and ZnO nanoparticles, deposited onto a PET/ITO substrate, where the ITO functions as the bottom electrode. For the top electrode, tungsten circular electrodes were deposited on top of the active layer.

During fabrication various parameters were studied, namely the concentration of nanoparticles in the PMMA solution and their size, and the spin-coating parameters. The effect of depositing the tungsten circular electrode with sputtering or using the tungsten microtip as top electrode was also considered. Regarding the spin-coating parameters, the best I-V behavior was achieved at 500 rpm for 30 s and 1000 rpm for 10 s. When it comes to the different

concentration of nanoparticles, it was found that a higher one improves the RS behavior of the devices when flat, but its behavior is worse with bent measurements. Analysing the difference in the nanoparticles size, it was observed that the bigger particles (100 nm) performed better in flat and bent measurements, comparing to the smaller ones. The deposition of the circular electrodes, although not making a difference in flat measurements, proved to leave the device more robust, especially when folded.

The final devices, were produced with the conditions that allowed better results after testing with all the varying parameters. They had 11% concentration of nanoparticles (ZnO or TiO_2) and the same curing time (60º C for 1h), however, the sample embedded with ZnO was deposited at 500 rpm for 30 s, with 1000 rpm/s of acceleration, whereas for the TiO_2 case, the velocity was 1000 rpm, spin-coated for 10 s at 2000 rpm/s of acceleration, implying a thinner active layer.

A few characterization techniques were used, namely XRD, SEM, profilometer and an optical microscope were applied to analyse the composition and surface morphology of the devices. To investigate further into the RS behavior of the devices, a set of electrical measurements was conducted using tungsten microtips, a Keithley 2400 SourceMeter and Arc One hardware platform to understand the functionality and behavior of the devices.

In the devices produced both with ZnO or $TiO_{2,}$ resistive switching (RS) was achieved under applied voltage for flat and bent configurations (30º and 60º folding configurations). These devices exhibited bipolar RS behavior, with SET at negative voltage and RESET at positive. This means that the resistance could be changed from high to low or vice versa, depending on the polarity of the applied voltage. Furthermore, the devices displayed RS characteristics of the valence change mechanism (VCM). In both devices it was clear that the folding configuration promotes an increase in the current, most likely because it makes the deposited layer thinner due to the bending. Comparing the performances in both devices, it was found that the TiO_2 devices was overall capable of higher resistance switches and current response comparing to the ZnO ones.

After demonstrating the presence of resistive switching (RS) in the devices and analysing their behavior, their endurance, retention and neuromorphic properties were assessed. Regarding the endurance of the devices when flat, the ZnO presented more stable results, however, the resistance gap between states proved to be, once again, smaller than the TiO_2 device. The endurance of the ZnO device seemed to worsen with folding configurations, whereas for the TiO_2 one the opposite occurred. This might mean that a thinner layer in this device is favorable for its endurance, once with folding measurements the layer seemed to get thinner, while for the ZnO one it seems to be detrimental. An analysis of the retention of the devices proved that when flat it was very adequate, even though the ZnO device presented more instability. The devices were overall considered to be non-volatile when flat and bent, once they were able to maintain the resistance state they were set to. Additionally the 60º bend also seemed to improve this characteristic in both devices, most likely due to the favorable thinning of layer, promoted by the folding configuration.

Furthermore, an analysis to the neuromorphic properties of the devices was performed. The ZnO sample in its flat state and the TiO_2 sample when folded at 60º exhibit promising outcomes in this regard. They demonstrate evident long-term potentiation (LTP) and long-term depression (LDP), which are essential aspects of the learning process. Because the devices produced needed higher voltages than the order of magnitude of neural signals to present RS, their validation with neural signals could not be implemented in due course. However, as a

future work, the process used to test their neuromorphic capabilities would be to simply use neural signals data and apply the voltage to the terminals of the device, after converting to the appropriate voltage range, and measuring its response.

Overall, it can be said that both devices have the capability to be implemented for their intended use, once they showed promising results when it comes to their RS behavior. However, it is important to address certain flaws that have been identified in order to further enhance their performance. One significant aspect that requires improvement is the behavior of the devices when subjected to bending or flexing. As the devices are intended to be flexible, it is essential to ensure that their performance remains stable even in bent configurations. The observed neuromorphic behavior is a key area that demands attention and improvement. Furthermore, it would be interesting to do additional tests such as electrical measurements under varying temperature to better understand the underlying phenomena responsible for the RS behavior.

The development of flexible resistive switching devices represents a significant breakthrough for neuromorphic applications, offering enhanced adaptability and interface capabilities with the soft tissues of the human body. By overcoming the limitations of rigid devices, these flexible devices hold tremendous potential for revolutionizing the field of neuroprosthetics. Moreover, the findings of this study contribute to the advancement of personalized and effective neuromorphic devices, with far-reaching implications for various AI applications beyond neuroprosthetics. The learning capabilities and flexibility of these devices enable their application in diverse fields, such as robotics, computer vision, natural language processing, and autonomous systems. The synergy between neuromorphic devices and AI algorithms promises to propel the development of intelligent systems that can learn, adapt, and interact with their environment in a more human-like and efficient manner. Another advantage of these devices for future applications is their transparency to light and the interesting light interaction coming from ZnO and TiO_2 nanoparticles, that could be useful in smart optoelectronics.

Página em branco

References

[1] H. Bao *et al.*, 'Toward memristive in-memory computing: principles and applications', *Frontiers of Optoelectronics*, vol. 15, no. 1. p. 23, 2022.

[2] A. Sebastian, M. Le Gallo, R. Khaddam-Aljameh, and E. Eleftheriou, 'Memory devices and applications for in-memory computing', *Nat. Nanotechnol. 2020 157*, vol. 15, no. 7, pp. 529–544, 2020.

[3] S. H. Jo, T. Chang, I. Ebong, B. B. Bhadviya, P. Mazumder, and W. Lu, 'Nanoscale memristor device as synapse in neuromorphic systems', *Nano Lett.*, vol. 10, no. 4, pp. 1297–1301, 2010.

[4] M.-J. Park, Y. Park, and J.-S. Lee, 'Solution-Processed Multiterminal Artificial Synapses Based on Ion-Doped Solid Electrolytes', *Cite This ACS Appl. Electron. Mater*, vol. 2020, pp. 339–345, 2020.

[5] H. Yuk, B. Lu, and X. Zhao, 'Hydrogel bioelectronics', *Chem. Soc. Rev.*, vol. 48, no. 6, pp. 1642–1667, 2019.

[6] C. Dias *et al.*, 'Bipolar resistive switching in Si/Ag nanostructures', *Appl. Surf. Sci.*, vol. 424, pp. 122–126, 2017.

[7] H. Wang *et al.*, 'Fabrication of Flexible Resistive Switching Devices Based on Lead-Free All-Inorganic CsSnBr3 Perovskite Using a One-Step Chemical Vapor Deposition Method', *Adv. Electron. Mater.*, vol. 6, no. 11, 2020.

[8] M. M. Rehman *et al.*, 'Biomaterial-Based Nonvolatile Resistive Memory Devices toward Ecofriendliness and Biocompatibility', *ACS Appl. Electron. Mater.*, vol. 3, no. 7, pp. 2832–2861, 2021.

[9] 'Beyond von Neumann', *Nature Nanotechnology*, vol. 15, no. 7. p. 507, 2020.

[10] L. O. Chua, 'Memristor—The Missing Circuit Element', *IEEE Trans. Circuit Theory*, vol. 18, no. 5, pp. 507–519, 1971.

[11] D. B. Strukov, G. S. Snider, D. R. Stewart, and R. S. Williams, 'The missing memristor found', *Nature*, vol. 453, no. 7191, pp. 80–83, 2008.

[12] S. Mao, B. Sun, G. Zhou, T. Guo, J. Wang, and Y. Zhao, 'Applications of biomemristors in next generation wearable electronics', *Nanoscale Horizons*, vol. 7, no. 8, pp. 822–848, 2022.

[13] A. G. Alharbi and M. H. Chowdhury, *Memristor Emulator Circuits*, 1st ed. Switzerland: Springer, 2021, pp. 9.

[14] F. Argall, 'Switching phenomena in titanium oxide thin films', *Solid State Electron.*, vol. 11, no. 5, pp. 535–541, 1968.

[15] D. B. Strukov, G. S. Snider, D. R. Stewart, and R. S. Williams, 'The missing memristor found', *Nature*, vol. 453, no. 7191, pp. 80–83, 2008.

[16] G. Milano *et al.*, 'Quantum Conductance in Memristive Devices: Fundamentals, Developments, and Applications', *Advanced Materials*, vol. 34, no. 32. John Wiley and Sons Inc, 2022.

[17] Z. Wen and D. Wu, 'Ferroelectric Tunnel Junctions: Modulations on the Potential Barrier', *Adv. Mater.*, vol. 32, no. 27, 2020.

[18] M. Patel, J. Gosai, N. Chaudhari, and A. Solanki, 'Hybrid Perovskite-Based Flexible and Stable Memristor by Complete Solution Process for Neuromorphic Computing', *Adv.*

Electron. Mater., vol. 9, no. 4, pp. 2200–2207, 2023.
[19] I. Boybat *et al.*, 'Neuromorphic computing with multi-memristive synapses', *Nat. Commun.*, vol. 9, no. 1, 2018.
[20] S. Dai *et al.*, 'Recent Advances in Transistor-Based Artificial Synapses', *Adv. Funct. Mater.*, vol. 29, no. 42, p. 1903700, 2019.
[21] A. Serb *et al.*, 'Memristive synapses connect brain and silicon spiking neurons', *Sci. RepoRtS |*, vol. 10, p. 2590, 2020.
[22] E. Juzekaeva *et al.*, 'Coupling Cortical Neurons through Electronic Memristive Synapse', *Adv. Mater. Technol.*, vol. 4, no. 1, 2019.
[23] I. Gupta, A. Serb, A. Khiat, R. Zeitler, S. Vassanelli, and T. Prodromakis, 'Real-time encoding and compression of neuronal spikes by metal-oxide memristors', *Nat. Commun. 2016 71*, vol. 7, no. 1, pp. 1–9, 2016.
[24] Z. Liu *et al.*, 'Neural signal analysis with memristor arrays towards high-efficiency brain–machine interfaces', *Nat. Commun.*, vol. 11, no. 1, 2020.
[25] C. Dias, D. Castro, M. Aroso, J. Ventura, and P. Aguiar, 'Memristor-Based Neuromodulation Device for Real-Time Monitoring and Adaptive Control of Neuronal Populations', *ACS Appl. Electron. Mater.*, vol. 4, no. 5, pp. 2380–2387, 2022.
[26] Y. Park and J. S. Lee, 'Flexible Multistate Data Storage Devices Fabricated Using Natural Lignin at Room Temperature', *ACS Appl. Mater. Interfaces*, vol. 9, no. 7, pp. 6207–6212, 2017.
[27] J. X. Zhu *et al.*, 'Flexible, transferable and conformal egg albumen based resistive switching memory devices', *RSC Adv.*, vol. 7, no. 51, pp. 32114–32119, 2017.
[28] N. Raeis-Hosseini and J. S. Lee, 'Controlling the Resistive Switching Behavior in Starch-Based Flexible Biomemristors', *ACS Appl. Mater. Interfaces*, vol. 8, no. 11, pp. 7326–7332, 2016.
[29] S. P. Park, Y. J. Tak, H. J. Kim, J. H. Lee, H. Yoo, and H. J. Kim, 'Analysis of the Bipolar Resistive Switching Behavior of a Biocompatible Glucose Film for Resistive Random Access Memory', *Adv. Mater.*, vol. 30, no. 26, 2018.
[30] Q. Shi, J. Wang, I. Aziz, and P. S. Lee, 'Stretchable and Wearable Resistive Switching Random-Access Memory', *Adv. Intell. Syst.*, vol. 2, no. 7, p. 2000007, 2020.
[31] E. Gale, 'TiO2-based memristors and ReRAM: Materials, mechanisms and models (a review)', *Semicond. Sci. Technol.*, vol. 29, no. 10, 2014.
[32] M. H. Tang *et al.*, 'Bipolar and unipolar resistive switching behaviors of sol–gel-derived SrTiO3 thin films with different compliance currents', *Semicond. Sci. Technol.*, vol. 26, no. 7, p. 075019, 2011.
[33] X. Sun, G. Li, X. Zhang, L. Ding, and W. Zhang, 'Coexistence of the bipolar and unipolar resistive switching behaviours in Au/SrTiO3/Pt cells', *J. Phys. D. Appl. Phys.*, vol. 44, no. 12, p. 125404, 2011.
[34] L. Goux, J. G. Lisoni, M. Jurczak, D. J. Wouters, L. Courtade, and C. Muller, 'Coexistence of the bipolar and unipolar resistive-switching modes in NiO cells made by thermal oxidation of Ni layers', *J. Appl. Phys.*, vol. 107, no. 2, p. 024512, 2010.
[35] R. Yasuhara *et al.*, 'Inhomogeneous chemical states in resistance-switching devices with a planar-type Pt/CuO/Pt structure', *Appl. Phys. Lett.*, vol. 95, no. 1, p. 012110, 2009.
[36] W. Y. Chang, Y. C. Lai, T. B. Wu, S. F. Wang, F. Chen, and M. J. Tsai, 'Unipolar resistive switching characteristics of ZnO thin films for nonvolatile memory applications', *Appl. Phys. Lett.*, vol. 92, no. 2, p. 022110, 2008.
[37] S. Zhang, S. Long, W. Guan, Q. Liu, Q. Wang, and M. Liu, 'Resistive switching characteristics of MnOx-based ReRAM', *J. Phys. D. Appl. Phys.*, vol. 42, no. 5, p. 055112, 2009.
[38] F. Miao *et al.*, 'Anatomy of a nanoscale conduction channel reveals the mechanism of a high-performance memristor', *Adv. Mater.*, vol. 23, no. 47, pp. 5633–5640, 2011.
[39] Y. Yang, P. Sheridan, and W. Lu, 'Complementary resistive switching in tantalum oxide-based resistive memory devices', *Appl. Phys. Lett.*, vol. 100, no. 20, p. 203112, 2012.
[40] A. S. Oblea, A. Timilsina, D. Moore, and K. A. Campbell, 'Silver chalcogenide based memristor devices', in *Proceedings of the The 2010 International Joint Conference on Neural Networks (IJCNN)*, 2010, pp. 1–3.
[41] F. Zeng *et al.*, 'Opportunity of the Lead-Free All-Inorganic Cs3Cu2I5 Perovskite Film for Memristor and Neuromorphic Computing Applications', *ACS Appl. Mater. Interfaces*, vol.

12, no. 20, pp. 23094–23101, 2020.
[42] C. Zhang, Y. Li, C. Ma, and Q. Zhang, 'Recent Progress of Organic–Inorganic Hybrid Perovskites in RRAM, Artificial Synapse, and Logic Operation', *Small Sci.*, vol. 2, no. 2, p. 2100086, 2022.
[43] S. Ali, S. Khan, A. Khan, and A. Bermak, 'Memristor Fabrication through Printing Technologies: A Review', *IEEE Access*, vol. 9. pp. 95970–95985, 2021.
[44] Z. Shen *et al.*, 'Memristive Non-Volatile Memory Based on Graphene Materials', *Micromachines 2020, Vol. 11, Page 341*, vol. 11, no. 4, p. 341, 2020.
[45] H. J. Gogoi, K. Bajpai, A. T. Mallajosyula, and A. Solanki, 'Advances in Flexible Memristors with Hybrid Perovskites', *J. Phys. Chem. Lett.*, vol. 12, no. 36, pp. 8798–8825, 2021.
[46] J. H. Heo, D. H. Shin, M. L. Lee, M. G. Kang, and S. H. Im, 'Efficient Organic-Inorganic Hybrid Flexible Perovskite Solar Cells Prepared by Lamination of Polytriarylamine/CH3NH3PbI3/Anodized Ti Metal Substrate and Graphene/PDMS Transparent Electrode Substrate', *ACS Appl. Mater. Interfaces*, vol. 10, no. 37, pp. 31413–31421, 2018.
[47] K. Ahn *et al.*, 'Flexible high-efficiency CZTSSe solar cells on stainless steel substrates', *J. Mater. Chem. A*, vol. 7, no. 43, pp. 24891–24899, 2019.
[48] G. Macrelli, A. K. Varshneya, and J. C. Mauro, 'Ultra-thin glass as a substrate for flexible photonics', *Opt. Mater. (Amst).*, vol. 106, p. 109994, 2020.
[49] Z. Qin *et al.*, 'Development of flexible paper substrate sensor based on 2D WS2 with S defects for room-temperature NH3 gas sensing', *Appl. Surf. Sci.*, vol. 573, p. 151535, 2022.
[50] Y. Xu *et al.*, 'Paper-based wearable electronics', *iScience*, vol. 24, no. 7, p. 102736, 2021.
[51] S. M. Khan, J. M. Nassar, and M. M. Hussain, 'Paper as a Substrate and an Active Material in Paper Electronics', *ACS Appl. Electron. Mater.*, vol. 3, no. 1, pp. 30–52, 2021.
[52] C. Dias, D. C. Leitao, C. S. R. Freire, H. L. Gomes, S. Cardoso, and J. Ventura, 'Resistive switching of silicon-silver thin film devices in flexible substrates', *Nanotechnology*, vol. 31, no. 13, p. 135702, 2020.
[53] X. Yan *et al.*, 'Flexible memristors as electronic synapses for neuro-inspired computation based on scotch tape-exfoliated mica substrates', *Nano Res.*, vol. 11, no. 3, pp. 1183–1192, 2018.
[54] J. M. Kim *et al.*, 'Effect of CdSe nanoparticles in polymethylmethacrylate tunneling layer on the performance of nonvolatile organic memory device', *Microelectron. Eng.*, vol. 98, pp. 305–308, 2012.
[55] A. H. Jaafar *et al.*, 'Polymer/TiO2Nanorod Nanocomposite Optical Memristor Device', *J. Phys. Chem. C*, vol. 125, no. 27, pp. 14965–14973, 2021.
[56] J. Mangalam, S. Agarwal, A. N. Resmi, M. Sundararajan, and K. B. Jinesh, 'Resistive switching in polymethyl methacrylate thin films', *Org. Electron.*, vol. 29, pp. 33–38, 2016.
[57] B. Pradhan, S. K. Majee, S. K. Batabyal, and A. J. Pal, 'Electrical bistability in zinc oxide nanoparticle-polymer composites', *J. Nanosci. Nanotechnol.*, vol. 7, no. 12, pp. 4534–4539, 2007.
[58] A. H. Jaafar, C. Lowe, A. Gee, and N. T. Kemp, 'Optoelectronic Switching Memory Based on ZnO Nanoparticle/Polymer Nanocomposites', *ACS Appl. Polym. Mater.*, vol. 5, no. 4, pp. 2367–2373, 2022.
[59] J. J. L. Hmar, 'Flexible resistive switching bistable memory devices using ZnO nanoparticles embedded in polyvinyl alcohol (PVA) matrix and poly(3,4-ethylenedioxythiophene) polystyrene sulfonate (PEDOT:PSS)', *RSC Adv.*, vol. 8, no. 36, pp. 20423–20433, 2018.
[60] C. Zhang, P. L. Yu, Y. Li, and J. C. Li, 'Polymer/TiO2 Nanoparticles interfacial effects on resistive switching under mechanical strain', *Org. Electron.*, vol. 77, pp. 1566–1199, 2020.
[61] D. O. Schmidt *et al.*, 'Resistive Switching of Individual, Chemically Synthesized TiO2 Nanoparticles', *Small*, vol. 11, no. 48, pp. 6444–6456, 2015.
[62] R. Tian *et al.*, 'Resistance switching characteristics of Ag/ZnO/graphene resistive

random access memory', *Vacuum*, vol. 207, p. 111625, 2023.
[63] L. Yang, *Resistive switching in TiO2 thin films*, 7th ed. Forschungszentrum Jülich GmbH, 2011.
[64] R. W. Chuang, C. C. Shih, and C. L. Huang, 'The enhanced electrode-dependent resistive random access memory based on BiFeO3', *Appl. Phys. A Mater. Sci. Process.*, vol. 129, no. 5, pp. 1–14, 2023.
[65] M. C. Hacker, J. Krieghoff, and A. G. Mikos, 'Synthetic Polymers', in *Principles of Regenerative Medicine*, Academic Press, 2018, pp. 559–590.
[66] J. Selvakumaran, M. P. Hughes, D. J. Ewins, and P. R. Richards, 'Biocompatibility studies of materials used for chronically implantable microelectrodes', in *1st Annual International IEEE-EMBS Special Topic Conference on Microtechnologies in Medicine and Biology - Proceedings*, 2000, pp. 521–525.
[67] T. Çaykara, M. G. Sande, N. Azoia, L. R. Rodrigues, and C. J. Silva, 'Exploring the potential of polyethylene terephthalate in the design of antibacterial surfaces', *Med. Microbiol. Immunol.*, vol. 209, no. 3, pp. 363–372, 2020.
[68] V. Nain, M. Kaur, K. S. Sandhu, R. Thory, and A. Sinhmar, 'Development, characterization, and biocompatibility of zinc oxide coupled starch nanocomposites from different botanical sources', *Int. J. Biol. Macromol.*, vol. 162, pp. 24–30, 2020.
[69] F. López-Huerta *et al.*, 'Biocompatibility and surface properties of TiO2 thin films deposited by DC magnetron sputtering', *Materials (Basel).*, vol. 7, no. 6, pp. 4105–4117, 2014.
[70] M. Ş. Kurt, M. E. Arslan, A. Yazici, İ. Mudu, and E. Arslan, 'Tribological, biocompatibility, and antibiofilm properties of tungsten–germanium coating using magnetron sputtering', *J. Mater. Sci. Mater. Med.*, vol. 32, no. 1, pp. 1–12, 2021.
[71] Sigma Aldrich, 'Poly(methyl methacrylate) Mw 350,000'. [Online]. Available: https://www.sigmaaldrich.com/PT/en/product/aldrich/445746. [Accessed: 23-May-2023].
[72] Sigma Aldrich, 'Zinc oxide nanopowder, particle size 100nm '. [Online]. Available: https://www.sigmaaldrich.com/PT/en/product/aldrich/544906. [Accessed: 23-May-2023].
[73] US Research Nanomaterials, 'Titanium Oxide Nanopowder (TiO2, rutile, high purity, 99.9+%, 30nm)'. [Online]. Available: https://www.us-nano.com/inc/sdetail/276. [Accessed: 23-May-2023].
[74] Sigma Aldrich, 'Titanium(IV) oxide, mixture of rutile and anatase nanopowder, particle size 100nm BET'. [Online]. Available: https://www.sigmaaldrich.com/PT/en/product/aldrich/634662. [Accessed: 23-May-2023].
[75] Sigma Aldrich, 'Indium tin oxide coated PET '. [Online]. Available: https://www.sigmaaldrich.com/PT/en/product/aldrich/639303. [Accessed: 23-May-2023].
[76] N. G. Semaltianos, 'Spin-coated PMMA films', *Microelectronics J.*, vol. 38, no. 6–7, pp. 754–761, 2007.
[77] H. Wang, F. Sun, C. Wang, Y. Zhu, and H. Wang, 'A simple drop-casting approach to fabricate the super-hydrophobic PMMA-PSF-CNFs composite coating with heat-, wear- and corrosion-resistant properties', *Colloid Polym. Sci.*, vol. 294, no. 2, pp. 303–309, 2016.
[78] A. K. Singh, 'Experimental Methodologies for the Characterization of Nanoparticles', in *Engineered Nanoparticles*, Academic Press, 2016, pp. 125–170.
[79] M. Gumustas, C. T. Sengel-Turk, A. Gumustas, S. A. Ozkan, and B. Uslu, 'Effect of Polymer-Based Nanoparticles on the Assay of Antimicrobial Drug Delivery Systems', *Multifunct. Syst. Comb. Deliv. Biosensing Diagnostics*, pp. 67–108, 2017.
[80] ArC INSTRUMENTS, 'ArC One'. [Online]. Available: https://www.arc-instruments.co.uk/products/arc-one/. [Accessed: 23-May-2023].
[81] R. C. Malenka and M. F. Bear, 'LTP and LTD: An embarrassment of riches', *Neuron*, vol. 44, no. 1, pp. 5–21, 2004.
[82] M. Lanza *et al.*, 'Standards for the Characterization of Endurance in Resistive Switching Devices', *ACS Nano*, vol. 15, no. 11, pp. 17214–17231, 2021.
[83] S. Fujinawa, F. Kato, and S. Sugiyama, 'Development of fabrication process for shape-

controlled three-dimensional nanostructures', Ph.D. dissertation, Graduate School of Science and Engineering, Ritsumeikan University, Japan, 2008, pp. 5,6.

[84] A. Rohatgi, 'WebPlotDigitizer: Version 4.6', 2022. [Online]. Available: https://automeris.io/WebPlotDigitizer/citation.html. [Accessed: 11-Jun-2023].

[85] M. Jerry *et al.*, 'Ferroelectric FET analog synapse for acceleration of deep neural network training', in *Technical Digest - International Electron Devices Meeting, IEDM*, 2018, pp. 6.2.1-6.2.4.